Accepted to Phys. Fluids 10.1063/5.0172540

Large Eddy Simulations of Flow past an Inclined Circular Cylinder: Insights into the Three-dimensional Effect

Gen Li (李根)[1,2], Wenhua Li (李文华)[1,2], Marek Jan Janocha[3], Guang Yin (尹光)[3], Muk Chen Ong[3*]

[1]*Marine Engineering College, Dalian Maritime University, Dalian, China*

[2]*National Center for International Research of Subsea Engineering Technology and Equipment, Dalian Maritime University, Dalian, China*

[3]*Department of Mechanical and Structural Engineering and Materials Science, University of Stavanger, N-4036 Stavanger, Norway*

Abstract

The flow past an inclined cylinder is simulated using Large Eddy Simulations to study the three-dimensional wake flow effects on the forces on the cylinder at Re = 3900. Four inclination angles of $\alpha = 0^\circ$, 30°, 45° and 60° are considered. The validity of the independence principle (IP) at the four investigated angles is examined. The results suggest that IP can predict the vortex shedding frequency at $0^\circ \leq \alpha \leq 60^\circ$, while it fails to predict the drag, lift, and pressure coefficients variations because the three-dimensional effect is neglected for IP. A comprehensive analysis is performed to provide insights into the three-dimensional effects on the drag and lift forces caused by α. The flow velocities, the Reynolds stress and the spanwise characteristic length of the flow structures are discussed in detail. It is found that the recirculation length reaches its maximum at $\alpha = 45^\circ$, which results in the smallest drag coefficient and lift force amplitudes. The spanwise characteristic lengths of the vortices are similar for all cases, while spanwise traveling patterns are observed only for $\alpha > 0^\circ$. A force partitioning analysis is performed to quantify the correlations between the forces and the spanwise

[*] Author to whom correspondence should be addressed: muk.c.ong@uis.no

and cross-spanwise vortices. It reveals that for α = 30°, the drag force becomes dominated by the cross-spanwise vorticity. With the increasing α, the dominant contribution gradually changes from the cross-spanwise to the spanwise vorticity, and the cross-spanwise vorticity contribution to the drag force further becomes negative at α = 60°.

Keywords: Inclined cylinder; Independence principle; Force partitioning; Large Eddy Simulations

I. INTRODUCTION

Flow past a stationary circular cylinder can be encountered in many engineering applications, such as towing cables, subsea pipelines and suspension bridges. This problem is typically characterized by the Reynolds number $Re = U_\infty D/\nu$, where U_∞ is the free stream velocity, D is the cylinder's diameter, and ν is the kinematic viscosity of the fluid. For most engineering applications, Re is larger than 350. Above this threshold the three-dimensionality of the wake flow can be clearly observed, as explained in the work of Williamson.[1] The inclination angle α is the angle between the free-stream flow direction and the perpendicular plane of the cylinder axis. In the case of a vertical cylinder, where the cylinder is normal to the incoming flow α = 0°. However, in most realistic flow scenarios, the flow is not perfectly normal to the cylinder's main axis. Compared to the purely vertical case of α = 0°, the cylinder inclination results in the development of an axial flow traveling in the spanwise direction. The existence of this spanwise flow is the main factor that influences the three-dimensional wake flow and has a significant effect on important hydrodynamic phenomena such as vortex-induced vibration, heat transfer and vortex-induced noise.

The primary issue for flow past an inclined cylinder is the dynamics of the vortex shedding from the cylinder, which is a major factor affecting the flow-induced forces acting on the cylinder. Najafi *et al.*[2] conducted an experiment for the flow past an inclined cylinder at Re = 5000. They employed both flow visualization and velocity field sampling by particle image velocimetry (PIV) technique. They revealed two distinct wake flow patterns, depending on the range of inclination angle, one corresponding to $\alpha = 0^\circ \sim 20^\circ$ and the second corresponding to $\alpha = 35^\circ \sim 45^\circ$. The dependence of vortex structures on the angle of inclination was also investigated by Lam *et al.*[3] who used large eddy simulations (LES). The spanwise vortices were found to be shed obliquely from the cylinder in the cases of $\alpha > 45^\circ$ as revealed by the instantaneous wake patterns at different locations along the cylinder span. However, quantifying the shedding angle of vortices separating from an inclined cylinder is challenging because the vortex shedding and its orientation are not steady and difficult to quantificationally identify, especially at high Re and large α.[4] A feasible way to identify the vortex shedding pattern is to analyze the force variation on the cylinder. Yeo and Jones,[5,6] Hogan and Hall,[7] Lucor and Karniadakis,[8] Zhao *et al.*,[9] Wang *et al.*,[10] and Zhao *et al.*[11] presented the spatial-temporal contours of the pressure and lift coefficients on the cylinder. The results showed inclined stripes in the spatiotemporal domain at $\alpha \geq 30^\circ$, representing a spanwise traveling mode in the vortex shedding behind an inclined cylinder.

For flows past nominally two-dimensional bodies, such as circular cylinders with an infinite length, the correlation length in the spanwise direction is an important measurement for describing the three-dimensionalities in the near-wake. A higher spanwise correlation indicates that the vortex shedding tends to occur uniformly along the spanwise direction. A good understanding of the spanwise correlation is not only essential for predicting the spatial distribution of the vortical structures but also can be used to determine a proper spanwise length of the computational domain to achieve a reasonable balance between the computational cost and the size of the domain sufficient to capture the essential flow physics for numerical simulations. For a vertical cylinder within the subcritical flow regime approximately from $Re = 350$ to $Re = 3\times10^5$, the correlation length of $2D \sim 3D$ has been well documented and the spanwise length of $H/D = 4 \sim 6$ of the computational domain has been extensively adopted by numerous works, such as Kravchenko and Moin,[12] Lei *et al.*,[13] Prsic *et al.*,[14] Tian and Xiao,[15] Jiang and Cheng,[16] Janocha *et al.*[17] On the other hand, the spanwise correlation length of an inclined cylinder has rarely been studied. The numerical results in the study of Yeo and Jones[6] at $Re = 1.4\times10^5$ revealed that force fluctuations are still correlated within a finite length of $10D$ along the inclined cylinder. Based on the results of direct numerical simulations (DNS) by Zhao *et al.*,[9,18] the correlation length of the axial vortices at the angle of inclination $\alpha = 45°$ were measured to be $3.2D$ and $4.0D$ for $Re = 300$ and 400, while the correlation length for $Re \geq 500$ has not been confirmed as the vortex structures were not clearly identified. The spanwise flow characteristics of an infinite cylinder with both inclined and yawed angles at $Re = 5.3\times10^4$ were studied by Wang *et al.*[19] The time-averaged streamwise vortices indicated the length between two vortex cores is $1.8D$. The experiment at $Re = 5.61\times10^4$ in Hogan and Hall[7] quantitively proved that the correlation length decreases rapidly from $3.3D$ to $1.1D$ with α increasing from 0° to 30°. For larger angles of inclination, the spanwise characteristic length of the vortical structures has not been thoroughly investigated to the authors' knowledge.

In addition to the three-dimensional characteristics of the wake flow structures, it is also important to quantitatively investigate the variation of the vortex-induced forces acting on the cylinder with the angle of inclination. The independence principle (IP), also known as the cosine law, was proposed as an estimation method for hydrodynamic characteristics. This theory assumes that the force coefficients and the vortex shedding frequency are equivalent to those in the vertical cases when they are normalized by the velocity component perpendicular to the cylinder axis u_n, regardless of the inclination angle α. The application of IP can greatly simplify the analysis of flow past cylinders with an arbitrary angle of inclination. However, the validity of IP is still arguable. Zhao *et al.*[18,20] performed a DNS study on the inclined cylinder with $0° \leq \alpha \leq 60°$ at Reynolds numbers covering $100 \leq Re \leq 1000$. They found that the Strouhal number $St = fD/U_\infty$ (where f is the vortex shedding frequency) and the mean drag coefficient can be well represented by the IP when $\alpha \leq 30°$, while the root-mean-square lift coefficient is highly dependent on the varying α. Lam *et al.*[3] used LES to study the case of an inclined cylinder at $Re = 3900$. Their results suggested that the IP is valid up to $\alpha = 45°$, and a similar conclusion was also drawn by Liang *et al.*[21] at the same Re. Najafi *et al.*[2] and

Zhou *et al.*[22] conducted an experimental investigation on the wake characteristics of an inclined cylinder at Re = 5000 and Re = 7200, respectively. The Strouhal number St, as well as the directions of separated shear layers and the spanwise vortices, were found to obey the IP when $\alpha \leq 40^\circ \sim 45^\circ$, while other features, such as velocity components, were dependent on α. On the other hand, results reported by Hogan and Hall[7] support that the vortex shedding frequency of an inclined cylinder can be predicted using IP with reasonable accuracy only when $\alpha \leq 20^\circ$. The study at Re = 3900 using LES by Zhou *et al.*[23] also held the viewpoint that hydrodynamic force coefficients and Strouhal number predicted by LES do not agree with the values predicted using IP, despite that these results predicted by IP remain constant at $15^\circ \leq \alpha \leq 60^\circ$. Wang *et al.*[10] concluded that the IP can reasonably predict the Strouhal number and the pressure distribution at some parts of the cylinder surface, while the drag force was underpredicted with a similar magnitude for all inclination angles.

Marshell[24] pointed out that IP is basically a two-dimensional method and only considers the contribution of the velocity component normal to the cylinder axis u_n. This may explain the limited applicability of IP at higher angles of inclination and higher Reynolds numbers, where the three-dimensional effect induced by the axial flow in the spanwise direction of the cylinder cannot be ignored. Although the three-dimensional nature of the vortices has been widely studied, as mentioned above, including the characteristics of vortex shedding and spanwise instabilities in shear layers, its effect on the hydrodynamic forces remains unexplored. In this research, we aim to comprehensively study the spatial and temporal characteristics of the three-dimensional wake flow past an inclined cylinder and quantitively investigate the correlations between the force on the cylinder and the flow characteristics. These detailed quantitative conclusions have been rarely considered in the existing works to authors best acknowledge. Four inclination angles ranging from 0° to 60° are selected in this study. In such cases, the forces normal to the cylinder axis are anticipated to be more pronounced compared to situations where the inclination angles exceeding 60°. Therefore, those angles are of much engineering interests.[18] Three specific cases with the inclination angles of 30°, 45° and 60° are representative to show the variance in the wake flow behind the cylinder, and have been widely considered in the existing works.[9-11] In the first step, the coefficients normalized by u_n are discussed to verify the IP. The influence of the inclination angle on the three-dimensional effects in the wake is addressed by analyzing the velocity and the Reynolds stress distributions, anisotropy, and spanwise length scales of the wake vortices. Finally, to quantify the origin of the vortex-induced force at different angles of inclination, the vorticity field is decomposed into the spanwise and the cross-spanwise parts, and their respective contributions to the hydrodynamic forces are calculated. The rest of this paper is organized as follows. The numerical methods applied in this study are described in Section II. The convergence and validation studies are presented in Section III. The results and discussions of flow analyses at four angles of inclination are covered in Section IV. Section V summarizes the most important findings and conclusions of the present study.

II. NUMERICAL METHODS

A. Governing equations and numerical scheme

The present study focuses on the three-dimensional effects of the flow past an inclined cylinder within the subcritical regime, which encompasses a wide range of engineering applications.[25–27] The Reynolds number of Re = 3900 is concerned as it is one of the most thorough documented case.[3,17] Considering the computational cost and the result accuracy, the present numerical model adopts the large eddy simulation (LES) method due to the ability of this method to accurately resolve the turbulent structures in the flow. The fluid is assumed to be incompressible and viscous, which satisfies the filtered Navier-Stokes equations solved within an LES framework:

$$\frac{\partial \tilde{u}_i}{\partial x_i} = 0 \tag{1}$$

$$\frac{\partial \tilde{u}_i}{\partial t} + \frac{\partial \tilde{u}_i \tilde{u}_j}{\partial x_j} = -\frac{1}{\rho}\frac{\partial \tilde{p}}{\partial x_i} + \frac{\partial}{\partial x_j}\left(\upsilon \frac{\partial \tilde{u}_i}{\partial x_j} - \tau_{ij}\right) \tag{2}$$

where $\tilde{u}_i$ (i = 1, 2, 3) are the filtered velocity components in the x-, y- and z-axis directions; $\tilde{p}$ is the filtered pressure; t is time; ρ and υ represent the fluid density and kinematic viscosity, respectively; τ_{ij} is the sub-grid-scale (SGS) stress written as:

$$\tau_{ij} = \widetilde{u_i u_j} - \tilde{u}_i \tilde{u}_j \tag{3}$$

In this study, the SGS stress tensor is modeled by:

$$\tau_{ij} - \frac{1}{3}\delta_{ij}\tau_{kk} = -2\upsilon_{SGS}\tilde{S}_{ij} \tag{4}$$

where δ_{ij} is the Kronecker delta; the strain rate tensor $\tilde{S}_{ij}$ is represented by:

$$\tilde{S}_{ij} = \frac{1}{2}\left(\frac{\partial \tilde{u}_i}{\partial x_j} + \frac{\partial \tilde{u}_j}{\partial x_i}\right) \tag{5}$$

The sub-grid kinematic viscosity υ_{SGS} in Eq. (4) is calculated by the wall-adapting local eddy-viscosity (WALE) model proposed by Nicoud and Ducros:[28]

$$\upsilon_{SGS} = C_k \sqrt{k_{SGS}}\tilde{\Delta} \tag{6}$$

where coefficient C_k is set to 0.094 in this study; the filter width $\tilde{\Delta}$ is given based on the cube root of the cell volume:

$$\tilde{\Delta} = V_C^{1/3} \tag{7}$$

The definition of SGS kinematic energy k_{SGS} in Eq. (6) can be found in the works of Tian and Xiao.[15] The open-source code OpenFOAM is used to solve numerically the governing equations. The PISO algorithm is used to decouple pressure and velocity in this study. The spatial schemes for gradient, divergence, Laplacian, and interpolation are least squares, Gauss Linear, corrected Gauss linear, and linear, respectively. The backward Euler method is used for temporal integration.

B. Computational domain

The flow past an infinite cylinder with an angle of inclination α is simulated using a rectangular computational domain, as shown in **FIG. 1**. The domain size is $6D$ in height, $20D$ in width, and $35D$ in length. The side planes and the inlet boundary are $10D$ away from the axis of the cylinder. The distance between the outlet boundary and the axis of the cylinder is $25D$. In this study, the coordinate system is defined by locating the origin at the geometric center of the cylinder and fixing x, y, z axes to the streamwise, transverse, and spanwise directions at $\alpha = 0°$, respectively. Therefore, in the following discussion, u, v, w in the velocity vector **U** represent the velocity components in x-, y- and z-axis directions, respectively.

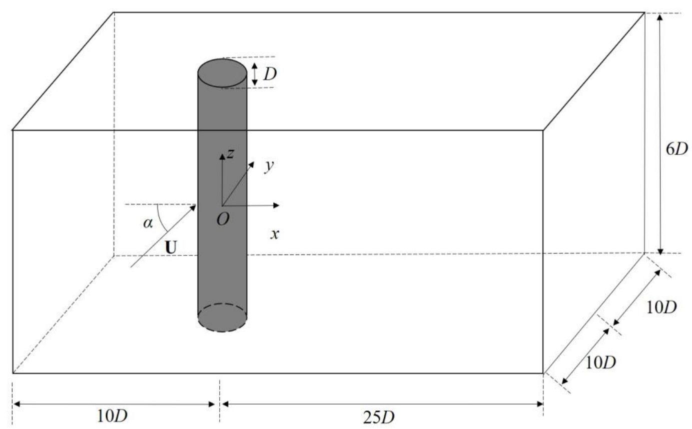

FIG. 1 Scheme diagram of computational domain.

The boundary conditions used in the simulations are as follows. The lateral boundaries parallel to the horizontal xy-plane are imposed with the periodic boundary conditions, and the symmetry boundary conditions are employed on the vertical planes parallel to the xz-plane. The non-slip boundary condition is set on the cylinder surface. The inlet boundary is specified with uniform flow $\mathbf{U} = (u, v, w) = (U_\infty \cos\alpha, 0, U_\infty \sin\alpha)$ and pressure gradient $\partial p/\partial n = 0$, while reference pressure $p=0$ and $\partial \mathbf{U}/\partial n = 0$ are set on the outlet boundary.

C. Lumley's triangle

To provide a quantitative description of the characteristic shape and the anisotropy of the vortices, the Lumley's triangle[29–33] anisotropy maps are used to analyze the flow past a cylinder with varying angles of inclination. This method introduces two invariants:

$$\eta^2 = -\mathrm{II}/3 \tag{8}$$

$$\xi^3 = \mathrm{III}/2 \tag{9}$$

where η and ξ are used to measure the anisotropy and the characteristic shape, respectively. II $= -a_{ij}a_{ij}/2$ and III $= a_{ij}a_{jk}a_{ik}/3$ are defined by the Reynolds stress anisotropy tensor:

$$a_{ij} = \overline{u_i'u_j'}/\overline{u_k'u_k'} - \delta_{ij}/3 \tag{10}$$

where u_i', u_j', u_k' refer to the velocity fluctuations in respective orthogonal directions. The three eigenvalues of the diagonalization of a_{ij} can then be used to describe the strength of velocity fluctuations.[34]

Lumley's triangle introduces a map constructed by the above invariants, which can be used to identify all realizable turbulence states. The physical definition of Lumley's triangle is introduced as follows. The left and right boundaries defined by $\eta = -|\xi|$ and $-1/6 \leq \xi \leq 1/3$ represent the axisymmetric turbulence structures, where the oblate-shaped turbulence with two major eigenvalues of the anisotropy tensor is located at the left boundary, and the prolate-shaped turbulence with only one major eigenvalue lies on the right boundary. The upper boundary refers to the essentially two-dimensional turbulence. In this state, the turbulent fluctuations are significant only in two directions. The three vertices of Lumley's triangle at right, left, and bottom represent the turbulence with the line shape of the one-dimensional feature, the disk shape with two-dimensional axisymmetric property, and the sphere shape with isotropy, respectively.

D. Hilbert transform

In this study, the spanwise length scales of three-dimensional wake structures are calculated using the Hilbert transform.[35] In comparison to the classical correlation length calculation based on the pressure fluctuation on the cylinder, the Hilbert transform can be used to characterize the temporal variations of the spanwise length scale and the amplitude along the cylinder span. The analytic representation of the vorticity component along a vertical line $\omega_y^a(z,t)$ can be written as:

$$\omega_y^a(z,t) = \omega_y(z,t) + i\mathcal{H}_{\omega_y}(z,t) = A_{\omega_y}(z,t)e^{i\Phi_{\omega_y}(z,t)} \tag{11}$$

where $i\mathcal{H}_{\omega_y}(z,t)$ is the Hilbert transform of $\omega_y^a(z,t)$; $A_{\omega_y}(z,t)$ is the temporal amplitude along the cylinder span; $\Phi_{\omega_y}(z,t)$ is the temporal phase. The spanwise length scale can be obtained with:

$$\lambda_z(z,t) = \frac{2\pi}{\frac{d}{dz}\Phi_{\omega_y}(z,t)} \tag{12}$$

The dominant wavelength can be obtained by calculating the probability density function (PDF) of length scales given by Eq. (12). A detailed description of this method can be found in Gsell *et al.*,[36] Sarwar and Mellibovsky[37], Ong and Yin[38], and Janocha *et al.*[17]

E. Force partitioning

As the angle of inclination increases, it is expected that the dominating component of vorticity in the wake region may also change, which consequently leads to differences in the development of vortex-induced forces. Therefore, one of the primary objectives of this paper is to characterize the orientation of the three-dimensional vortex structures behind a cylinder at different angles of inclination and further quantify the relationship between the flow structures and the forces on the cylinder. For this reason, the force partitioning method[39–43] is employed. This method simplifies a complex fluid flow problem by decomposing the total force into parts related to viscosity, vorticity and added mass.

Considering a stationary cylinder in uniform flow, the hydrodynamic force acting on the cylinder can be generally split into vorticity- and viscosity-induced parts:

$$F_i = F_i^{\omega} + F_i^{\nu} \tag{13}$$

where $i = x, y$ represents the drag and lift forces in the x and y directions; ω and ν denote the contribution of vorticity and viscosity, respectively. The vorticity-induced force can be represented by:

$$F_i^{\omega} = \rho \int_{V_f} \boldsymbol{\nabla} \cdot (\mathbf{U} \cdot \boldsymbol{\nabla}\mathbf{U}) \varphi_i dV = -\rho \int_{V_f} 2Q\varphi_i dV \tag{14}$$

where V_f denotes the entire fluid domain. The criterion Q is defined by:

$$Q = \frac{1}{2}(\|\boldsymbol{\Omega}\|^2 - \|\mathbf{S}\|^2) \tag{15}$$

where $\mathbf{\Omega}$ and $\mathbf{S}$ are the rotation rate and the strain rate tensors, respectively. Therefore, $Q > 0$ represents the rotational-dominant flow regions, and $Q < 0$ represents the strain-dominant flow regions. The auxiliary potential φ_i in Eq. (14) is assumed to satisfy the following governing equation and boundary conditions:

$$\nabla^2 \varphi_i = 0 \tag{16}$$

$$\mathbf{n} \cdot \boldsymbol{\nabla} \varphi_i = \begin{cases} n_i, & on\ \mathrm{B} \\ 0, & on\ \Sigma \end{cases} \tag{17}$$

where $\mathbf{n} = (n_x, n_y, n_z)$ is the unit normal vector on the cylinder surface; B is the cylinder surface; Σ are the outer boundaries, including inlet, outlet, side, and lateral walls. The viscosity-induced force F_i^{ν} in Eq. (13) can also be expressed using the auxiliary potential φ_i:

$$F_i^{\nu} = \mu \int_{V_f} (\boldsymbol{\nabla}^2 \mathbf{U}) \cdot \boldsymbol{\nabla} \varphi_i dV = -\mu \int_{V_f} \boldsymbol{\nabla} \cdot (\boldsymbol{\omega} \times \boldsymbol{\nabla} \varphi_i) dV = -\mu \oint_{\Sigma} (\mathbf{n} \times \boldsymbol{\omega}) \cdot \boldsymbol{\nabla} \varphi_i dS \tag{18}$$

where μ is the dynamic viscosity.

A further decomposition for F_i^{ω} is then performed to identify the dominant component of the vorticity. In this study, the vorticity orientation is quantified by the angle between the vorticity vector $\boldsymbol{\omega} = (\omega_x, \omega_y, \omega_z)$ and the z-axis:[43]

$$\eta_z = \frac{\omega_z}{|\boldsymbol{\omega}|} \tag{19}$$

By using this convention, the spanwise and cross-spanwise vortices can be distinguished by $|\eta_z| > \cos(\pi/4)$ and $|\eta_z| < \cos(\pi/4)$, respectively. The value of $|\eta_z|$ denotes that the magnitude of the angle between the local vorticity vector and the cylinder span is larger or smaller than 45°. **FIG. 2** shows the definition of spanwise and cross-spanwise directions. **FIG. 3** shows an example of the iso-surfaces of the vortex structures at $\alpha = 45°$ identified by $Q/(u_n^2/D^2) = 1$ corresponding to the spanwise and cross-spanwise vorticity fields, respectively. The contributions of spanwise and cross-spanwise vortices to the force can be quantified as:

$$F_i^{\omega} = F_i^{\omega z} + F_i^{\omega xy}$$

where $F_i^{\omega z}$ and $F_i^{\omega xy}$ denote the forces contributed by the spanwise and cross-spanwise vorticities, respectively.

After obtaining the force F_i, the corresponding force coefficient C_{in} can be calculated as:

$$C_{in} = \frac{F_i}{\frac{1}{2}\rho u_n^2 DH} \tag{20}$$

where ρ is fluid density; $H = 6D$ is the height of the cylinder; subscript n represents the coefficient normalized by normal velocity $u_n = U_\infty \cos\alpha$.

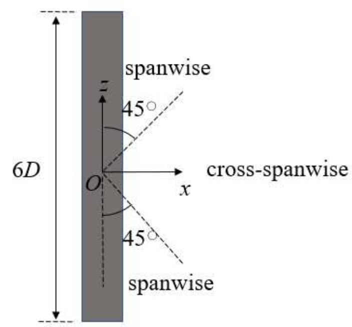

FIG. 2 Illustration of spanwise and cross-spanwise directions.

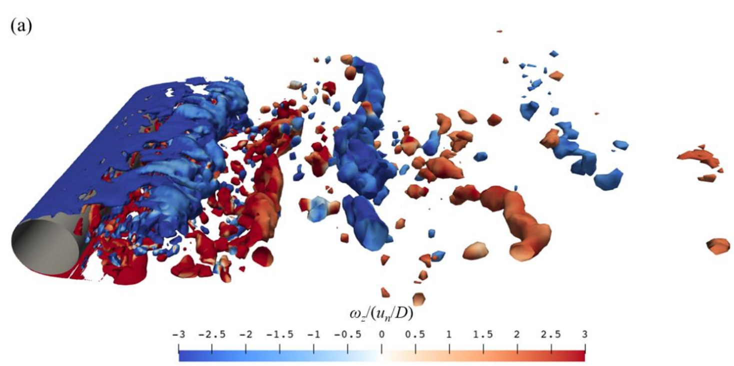

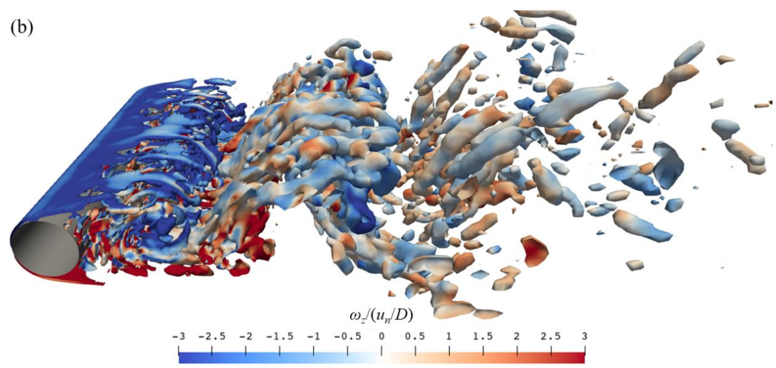

FIG. 3 Instantaneous iso-surfaces $Q/(u_n^2/D^2) = 1$ corresponding to (a) the spanwise and (b) the cross-spanwise vorticities.

III. CONVERGENCE AND VALIDATION STUDIES

A. Convergence study

The mesh topology adopted in this study is shown in **FIG. 4,** presenting the horizontal cross-section of the domain. The O-grid area surrounding the cylinder is formed by an overlap of four circles of 15D in diameter whose centers are 10D away from the cylinder axis. A number of 320 nodes are equally distributed on the circumference of the cylinder and radially extruded inside the O-grid zone. The first node next to the cylinder surface is placed according to the average dimensionless distance $y^+ = u_f h/\nu < 0.3$, where u_f is the friction velocity and h is the distance in the normal direction to the cylinder's surface. The mesh size increases in both x and y directions from the cylinder surface to the boundary of the O-grid zone. The meshes adjacent to the O-grid area smoothly transition to an H-grid topology and then gradually extrude to reduce the cell number away from the cylinder. The length of the longest cells in the far field is kept under 0.4D. In most studies on the flow past a vertical cylinder at $Re = 3900$ using LES, the spanwise resolution Δz is approximately from 0.047D to 0.065D.[12,16,17,44–46] The reported spanwise resolutions for the cases of an inclined cylinder at $Re = 3900$ range from 0.09D to 0.11D.[23,47] In this study, 96 layers of nodes are equally distributed along the spanwise direction of the computation domain to capture the axial flow, corresponding to $\Delta z = 0.063D$. The results are sampled over non-dimensional time $tu_n/D > 250$, covering at least 50 vortex-shedding periods.

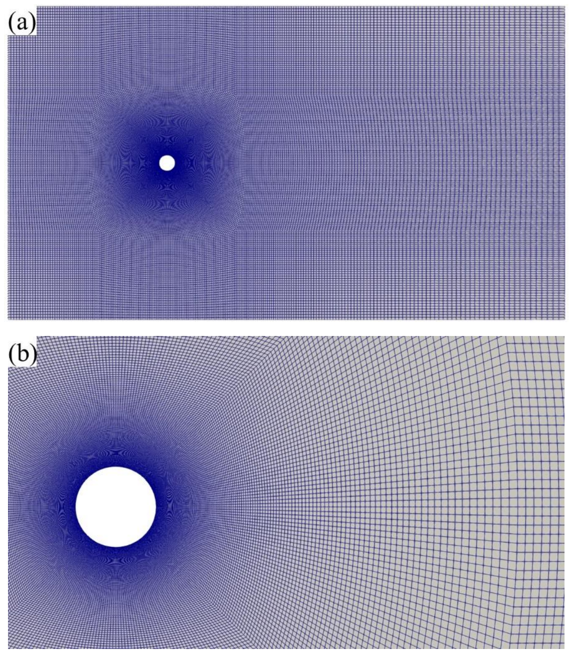

FIG. 4 Computational mesh topology in *xy*-plane: (a) entire domain and (b) close-up view of the mesh near the cylinder surface.

In the following discussion, all spanwise-averaged results are denoted by angle brackets $\langle\cdot\rangle$ and all time-averaged results are denoted with an overline $\overline{(\cdot)}$. **TABLE I** shows three flow cases around a cylinder at $\alpha = 0°$ for the mesh independence test. As the normal velocity $u_n = U_\infty$ at $\alpha = 0°$, the subscript n of all coefficients in the convergence studies is omitted. Three mesh schemes are used, where the cell number increases at a rate of approximately 30%. This increment is carried out by expanding the node number in the radial direction within the O-grid zone, progressing from 150 to 200 and eventually to 250. The mesh size in the O-grid zone increases at a ratio less than 1.02, to guarantee the dimensionless distance $y^+ < 0.3$ to the wall.

All three mesh variants give a similar Strouhal number $St = fD/U_\infty$ around 0.21, where f is the vortex shedding frequency. The average drag coefficient $\langle\overline{C_d}\rangle$, the root mean square of the lift coefficient $\langle C_l\rangle_{rms}$, the base pressure coefficient $-\langle\overline{C_{p_b}}\rangle$, the separation angle $\langle\overline{\theta_{sep}}\rangle$ and the recirculation length L_{rec} predicted by the simulation using the medium mesh M2 agree very well with those predicted by simulation using the finest mesh M3. A detailed mesh convergence study, including comparisons of velocity profiles and pressure distributions on the cylinder, can be found in **Appendix**. Based on the obtained results, it can be concluded that a reasonable mesh convergence is obtained by M2.

The convergence test for the time step Δt is then performed using mesh M2. **TABLE II** shows that St is independent of the time step size in the investigated range of Δt, and the rest of the results in the three cases are also close to each other. Considering the balance of accuracy and efficiency, the time step scheme T2 ($\Delta tU_\infty/D = 3.9\times10^{-3}$) is chosen for the remaining simulations.

TABLE I Results of mesh convergence test.

Case	Cell count	$\langle\overline{C_d}\rangle$	$\langle C_l\rangle_{rms}$	St	$-\langle\overline{C_{p_b}}\rangle$	$\langle\overline{\theta_{sep}}\rangle$	L_{rec}/D
M1	6.18×10^6	1.1352	0.3291	0.2115	1.0702	87.69°	1.11
M2	8.52×10^6	1.0580	0.1886	0.2179	0.9712	86.54°	1.31
M3	1.14×10^7	1.0527	0.1671	0.2191	0.9053	86.54°	1.31

TABLE II Results of time-step convergence test.

Case	$\Delta tU_\infty/D$	$\langle\overline{C_d}\rangle$	$\langle C_l\rangle_{rms}$	St	$-\langle\overline{C_{p_b}}\rangle$	$\langle\overline{\theta_{sep}}\rangle$	$\langle\overline{L_{rec}}\rangle/D$
T1	7.8×10^{-3}	1.0487	0.1947	0.2179	0.9330	87.69°	1.31
T2	3.9×10^{-3}	1.0580	0.1886	0.2179	0.9712	87.69°	1.31
T3	2.0×10^{-3}	1.0643	0.2269	0.2179	0.8911	87.69°	1.41

B. Validation study

1. Flow past a vertical cylinder

The simulation results of flow past a cylinder at $\alpha = 0°$ and $Re = 3900$ using mesh M2 and time step T2 are compared with available published data to validate the present numerical model. The pressure distribution on the cylinder surface, as shown in **FIG. 5**, is calculated by:

$$C_p = \frac{p - p_\infty}{\rho U_\infty^2/2} \tag{21}$$

where reference pressure p_∞ is set as the pressure at the inlet boundary. The pressure distribution on the cylinder surface is well captured by the present simulation compared to the direct-numerical-simulation (DNS) results reported by Ma *et al.*,[48] and the LES results in Kravchenko and Moin[12] and Janocha *et al.*[17] **FIG. 6** shows the averaged velocity component u at the center plane $y = 0$, where the present simulation agrees well with both the numerical and experimental data. **FIG. 7** gives the spanwise-averaged power spectra of velocity fluctuations at different x locations. Except for $x/D = 3$, all the other three plots of $x/D = 5$, 7 and 9 have been offset downwards by 10^{-3}, 10^{-6} and 10^{-9} for clarity, respectively. All the spectra follow Kolmogorov's $-5/3$ power law, indicating that the energy cascade of turbulent scales is captured by the present simulation. The comparisons of velocity and Reynolds stress components are shown in **FIG. 8** and **FIG. 9**, respectively. The transition of U-shape distribution of $\langle \bar{u} \rangle$ into V-shape is clearly visible in **FIG. 8** between the locations $x/D = 1.06$ and $x/D = 1.54$. Generally, a good agreement is found between the quantities predicted by the present model and the published data. Based on the validation study presented in **FIG. 5** to **FIG. 8**, the present numerical model is considered sufficient to resolve the turbulent flow features behind a vertical cylinder.

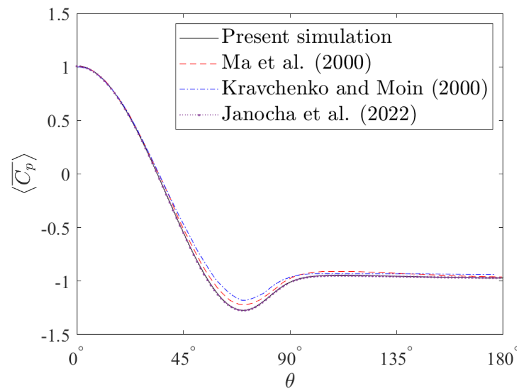

FIG. 5 Pressure coefficient $\langle \overline{C_{p_b}} \rangle$ on cylinder surface.

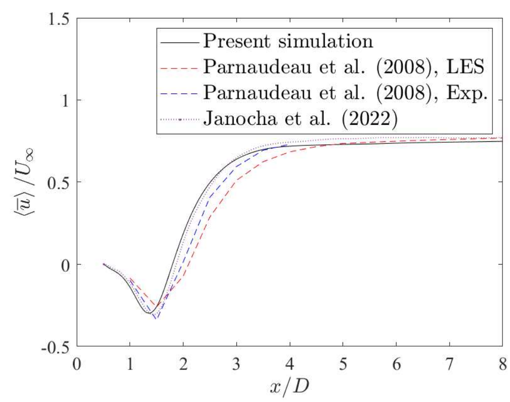

FIG. 6 Velocity component $\langle \overline{u} \rangle$ at $y = 0$.

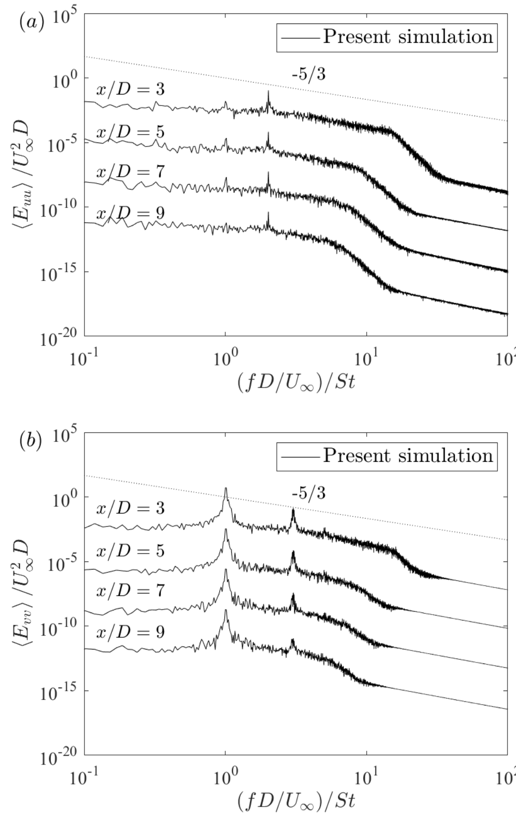

FIG. 7 Power spectra of velocity fluctuation at different locations of *x/D*: (a) $\langle E_{uu} \rangle$ in *x*-axis direction and (b) $\langle E_{vv} \rangle$ in *y*-axis direction.

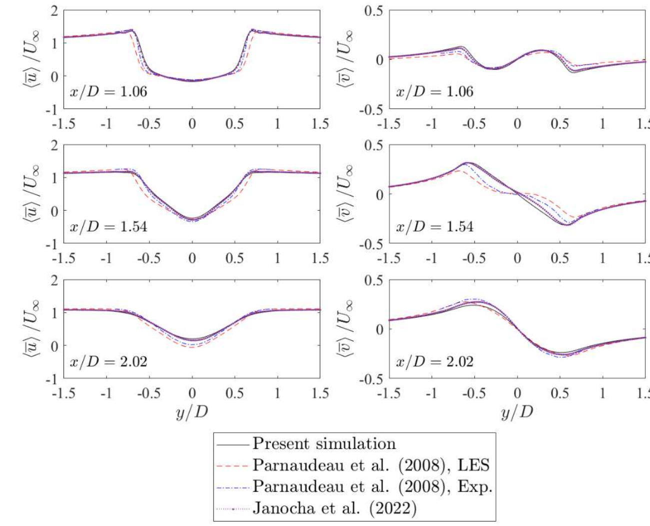

FIG. 8 Velocity components at different locations of *x/D*, left column is $\langle \bar{u} \rangle$ in *x*-axis direction and right column represents $\langle \bar{v} \rangle$ in *y*-axis direction.

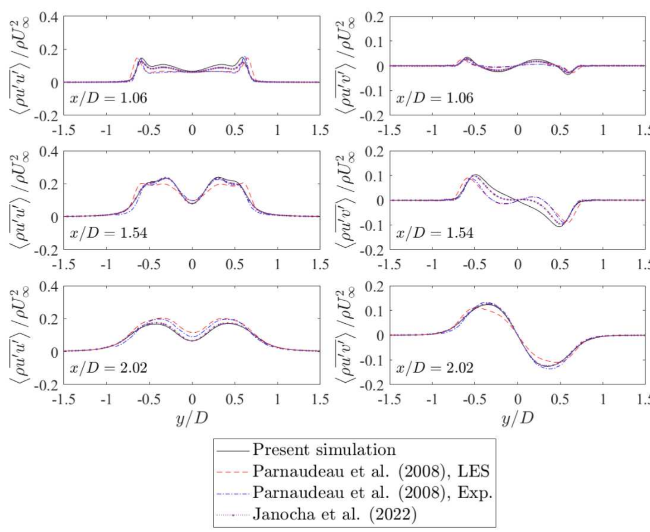

FIG. 9 Reynolds stress at different locations of *x/D*, left column is normal component $\langle \overline{u'u'} \rangle$ and right column is shear component $\langle \overline{u'v'} \rangle$.

2. Flow past an inclined cylinder

The flow past the cylinder at various angles of inclination is modelled by modifying the inlet boundary condition to represent the oblique flow instead of rotating the cylinder and remeshing the whole domain.[10,11] A general flow feature can be identified by analyzing the instantaneous streamlines of the flow around the cylinder. When the flow first reaches the cylinder with a non-zero angle of inclination, it moves a small distance along the cylinder span due to the velocity component $w > 0$. After that, the flow passes the cylinder obliquely upwards on both sides of the cylinder and then separates from the cylinder surface at the separation point (denoted by the dashed lines in **FIG. 10**). The axial flow is clearly visible in the near wake after the shear layer separates. **FIG. 10** shows the instantaneous streamlines with seed points distributed along the line $z/D = -3H$ in the plane $y/D = 0$ in three cases of $\alpha = 30°$, $45°$ and $60°$. The lower part of the cylinder is not traced due to the location of the seed points of the upstream streamlines. Despite this, the above-mentioned flow pattern behind an inclined cylinder is precisely reproduced by the present simulation, and similar patterns were also reported by Najafi *et al.*[2] and Lam *et al.*[3]

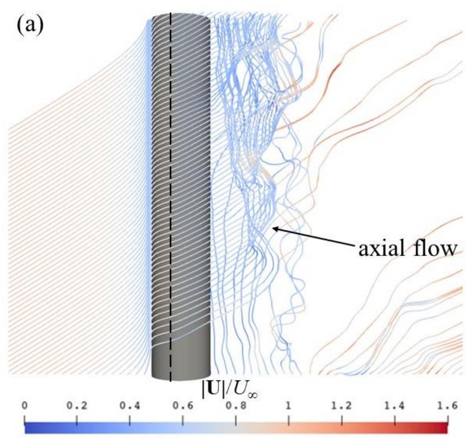

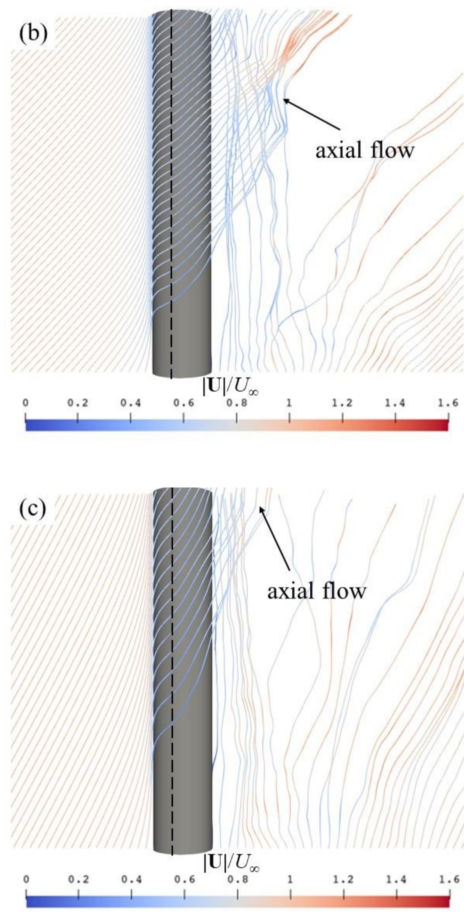

FIG. 10 Instantaneous streamlines: (a) $\alpha = 30°$, (a) $\alpha = 45°$ and (c) $\alpha = 60°$.

The magnitude of the velocity component in the streamwise direction is then compared with numerical and experimental results from Lam *et al.*[3] at *Re* = 3900 and Najafi *et al.*[2] at *Re* = 5000 to validate the present model. Different from the present simulation, those studies are conducted by placing the cylinder with an angle of inclination and presenting the results with a rotating coordinate:

$$\begin{cases} x' = x\cos\alpha + z\sin\alpha \\ y' = y \\ z' = -z\sin\alpha + z\cos\alpha \end{cases} \tag{22}$$

The relationship between the rotation coordinate *O-x'y'z'* and the present global coordinate *O-xyz* is shown in the schematic diagram in **FIG. 11**.

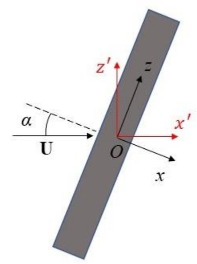

FIG. 11 Schematic diagram of the global coordinate *O-xyz* used in this paper and the rotating coordinate *O-x'y'z'* as reported by Lam *et al.*[3] and Najafi *et al.*[2]

As shown in **FIG. 12**, the time-averaged streamwise velocity component for two investigated α is sampled along the x'-axis direction at y' = 0 and *z/D* = 0, -1 and -2, respectively. $\overline{u_{x'}}$ is zero at the cylinder surface and then gradually increases to about 0.8*D* with the increasing x'. A local minimum caused by strong recirculation in the near wake is visible in each plot. As the flow characteristics are statistically homogeneous along the *z*-axis rather than z'-axis, a phase difference occurs inevitably at different *z*-locations. Despite this, the present simulation is able to capture the profile of $\overline{u_{x'}}$, as well as the velocity magnitude at the far field, in both investigated cases (α = 30° and 45°). The results of the present validation study support the ability of the present model to predict accurately $\overline{u_{x'}}$ profiles for inclined cylinder flow cases.

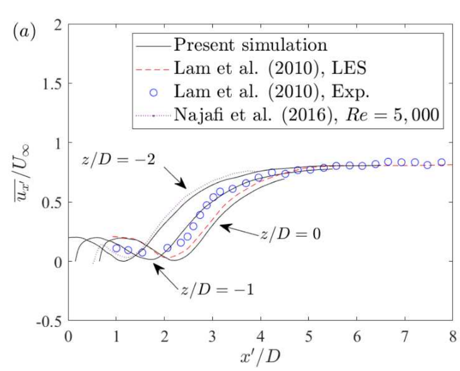

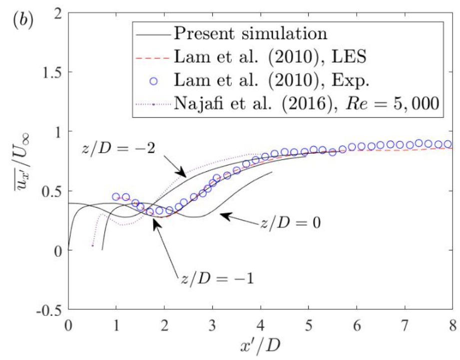

FIG. 12 Time-averaged streamwise velocity component $\overline{u_{x'}}$: (a) $\alpha = 30°$ and (b) $\alpha = 45°$.

IV. RESULTS AND DISCUSSION

A. Independence principle for force coefficients

The independence principle (IP) is a convenient approach for estimating the hydrodynamic features of flow past an inclined cylinder. It assumes that the features normalized by the velocity component perpendicular to the cylinder axis, $u_n = U_\infty \cos\alpha$, are independent of the angle of inclination α. To validate the applicability of IP the time- and spanwise-averaged coefficients, shown in **TABLE III**, are used to analyze the flow past a cylinder with different angles of inclination. The main objective of this study is to illustrate the detailed insights of the flow past an inclined cylinder, which can be widely seen in various engineering applications, such as towing cables, subsea pipelines, suspension bridges. The selected four angles ranging from 0° to 60° can cover most of those scenarios. The inclination angles 30°, 45° and 60° are also representative to show the differences in the wake flow of the cylinder, and have been widely concerned in the existing works. Therefore, those angles are selected in the present study.

In comparison with the vertical case of $\alpha = 0°$, the Strouhal number St_n is similar in all investigated cases. However, the normalized drag and lift coefficients $\langle \overline{C_{dn}} \rangle$ and $\langle C_{ln} \rangle_{rms}$ are lower in the inclined cases. The coefficient $\langle \overline{C_{zn}} \rangle$ of the spanwise force increases with the increasing angle of inclination. **FIG. 13** shows the pressure coefficient distribution on the surface of the cylinder, where θ is the angular coordinate with $\theta = 0^\circ$ being the stagnation point. Similar to the drag and lift forces, the normalized pressure distribution is similar in all three cases of $\alpha \geq 30^\circ$, while their magnitudes are smaller than that in the vertical case.

The present results show that St_n remains relative stable in all four cases, which indicates that IP can be used to reasonably predict the vortex shedding frequency. This conclusion is similar with those in the experimental study of Najafi *et al.*[2] and Zhou *et al.*[22] On the other hand, the drag coefficients $\langle\overline{C_{dn}}\rangle$ and lift coefficients $\langle C_{ln}\rangle_{rms}$ exist obvious differences between the vertical and inclined cases. This observation suggests the force predictions using IP are inaccurate, which agrees well with Zhou *et al.*[23] and Wang *et al.*[10] The discrepancy in force coefficient predictions by IP is because it only considers the contribution of the velocity in the 2D *xy*-plane. However, the flow three-dimensionality induced by the axial flow along the cylinder span should not be neglected when the angle of inclination is larger than 30°. The increasing importance of flow three-dimensionality is indicated by the increasing value of $\langle\overline{C_{zn}}\rangle$ with the increasing α. A detailed discussion of the three-dimensional effects is given in the following sub-sections.

TABLE III Averaged force coefficients at different angles of inclination.

α	$\langle\overline{C_{dn}}\rangle$	$\langle C_{ln}\rangle_{rms}$	$\langle\overline{C_{zn}}\rangle$	St_n
0°	1.0580	0.1949	0	0.2179
30°	0.9581	0.0707	0.0295	0.2153
45°	0.9509	0.0523	0.0569	0.2176
60°	0.9757	0.0769	0.1200	0.2103

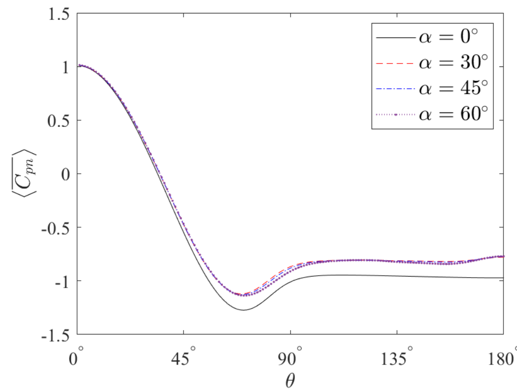

FIG. 13 Pressure coefficient distribution $\langle\overline{C_{pn}}\rangle$ on cylinders' surface at different angles of inclination.

FIG. 14 shows the spanwise-averaged drag and lift coefficients as a function of time, where low and high drag regimes are specified by $(\langle\overline{C_{dn}}\rangle + \langle C_{dn}\rangle_{\min})/2$ and $(\langle\overline{C_{dn}}\rangle + \langle C_{dn}\rangle_{\max})/2$, respectively. It should be clarified that $\langle C_{zn}\rangle$ does not show significant time variability throughout the present simulations, and it is not shown in the plots. In the case of $\alpha = 0°$, apparent low and high drag regimes are spotted, and these regimes are correlated with small and large amplitudes of the lift coefficient. Low and high drag regimes still exist in the inclination cases, but the differences between their magnitudes are much less noticeable. Those differences in the two regimes are consistent with the variance of $\langle C_{ln}\rangle_{rms}$ with α shown in **TABLE III**, where the smallest difference occurs at $\alpha = 45°$ and it is similar at $\alpha = 30°$ and $\alpha = 60°$. On the other hand, the frequency of the drag coefficient is approximately twice that of the lift coefficient in each case of α. This indicates that the periodic vortex shedding at both sides of the cylinder is still the main reason for the periodic variation in forces, regardless of whether the cylinder is vertical or inclined.

1
2
3

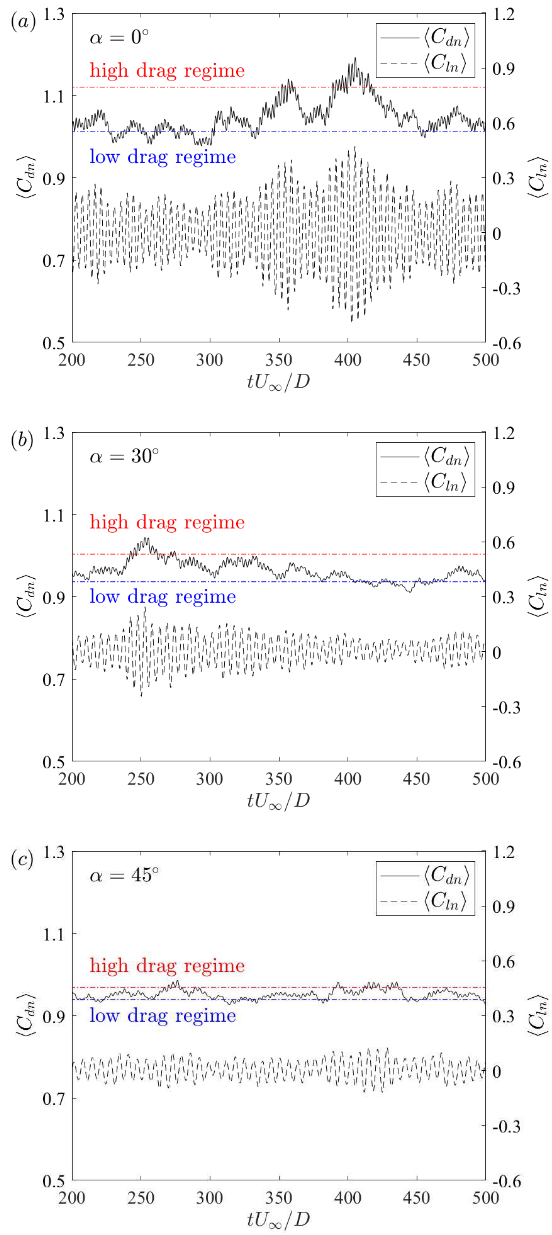
(a)
$\alpha = 0°$
$\langle C_{dn} \rangle$
$\langle C_{ln} \rangle$
high drag regime
low drag regime
tU_∞/D
(b)
$\alpha = 30°$
(c)
$\alpha = 45°$

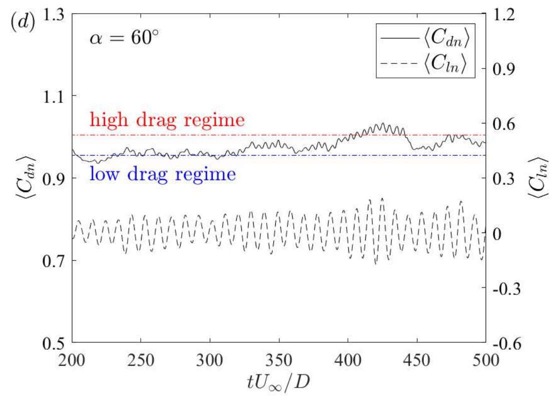

FIG. 14 Force coefficients of drag $\langle C_{dn} \rangle$ and lift $\langle C_{ln} \rangle$: (a) $\alpha = 0°$, (b) $\alpha = 30°$, (c) $\alpha = 45°$ and (d) $\alpha = 60°$.

In order to investigate the variation of vortex shedding frequency in both high and low regimes in all four cases, wavelet transform analysis is conducted to illustrate the amplitude St_n in the time series. **FIG. 15** shows the time-frequency representation of the lift coefficient after wavelet transform. The peak frequencies are distributed near St_n in all four cases, denoting that the vortex shedding frequency is temporally stable and is independent of the occurrence of low/high drag phenomenon. However, the enhancement and suppression in the amplitude can be observed corresponding to the high and low drag regimes and this amplitude modulation is attenuated with the increasing incline angle.

Accepted to Phys. Fluids 10.1063/5.0172540

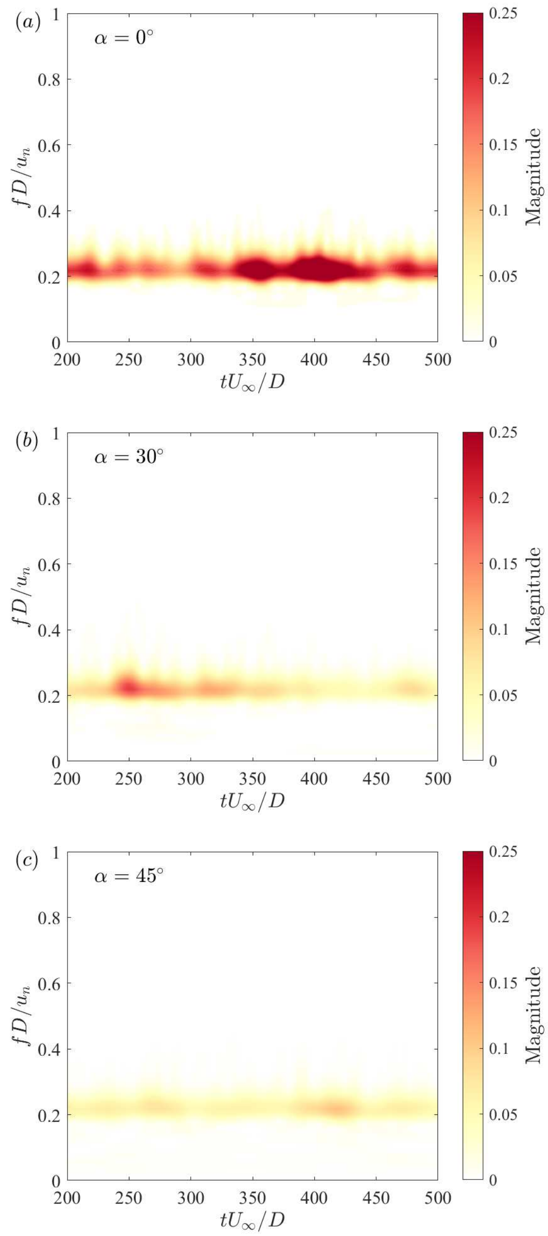

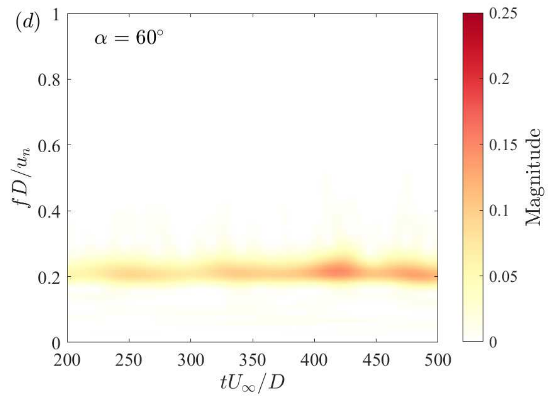

FIG. 15 Vortex shedding frequency f: (a) $\alpha = 0°$, (b) $\alpha = 30°$, (c) $\alpha = 45°$ and (d) $\alpha = 60°$.

The wall stress distribution indicates the fluid motion on the cylinder surface. Additionally, the separation of the boundary layer occurs at the point where the wall shear stress becomes zero. This separation phenomenon further impacts the subsequent vortex shedding behind the cylinder. Therefore, it is imperative to conduct a thorough investigation of the wall stress distribution on the cylinder surface. **FIGS. 16-17** present the time- and spanwise-averaged wall shear stress components normalized by U_∞ and u_n. Both components of wall shear stress distribution along the cylinder circumference vary significantly between different angles of inclination. **FIG. 16** shows that the magnitude of the tangential component represented by the magnitude of $|\langle\overline{\tau_{wx}}\rangle, \langle\overline{\tau_{wy}}\rangle|$ normalized by u_n at $\alpha = 30°$ is close to that in the vertical case, and increases significantly in $\alpha = 45°$ and $\alpha = 60°$ cases. This indicates that the flow characteristics remain relatively similar in the xy-plane between the cases of $\alpha = 0°$ and $\alpha = 30°$.

Considering the time-averaged spanwise component of shear stress $\langle\overline{\tau_{wz}}\rangle$, **FIG. 17** shows that $\langle\overline{\tau_{wz}}\rangle$ is zero only in the cases of $\alpha = 0°$, and the $\langle\overline{\tau_{wz}}\rangle$ values become nonzero for inclined cylinder cases due to spanwise flow. The spanwise flow is the main origin of enhanced three-dimensionality of inclined cylinders' near wake and decreased IP accuracy at large inclination angles. The largest magnitude of $\langle\overline{\tau_{wz}}\rangle$ is located at $\theta = 0°$ where the incoming flow reaches the cylinder, and it reduces with the increasing θ. After the normalization by u_n, the largest magnitude at this position is observed in the case of α = 60°, followed by α = 45° and α = 30°. This observation is consistent with the observation of streamlines in **FIG. 10**. Close to the separation point where $|\langle\overline{\tau_{wx}}\rangle, \langle\overline{\tau_{wy}}\rangle|$ being zero, the value of $\langle\overline{\tau_{wz}}\rangle$ reaches its minimum but remains greater than zero. After the separation point, the value of $\langle\overline{\tau_{wz}}\rangle$ continues to increase, and this increment is the most apparent in the case of α = 60° after the normalization by u_n.

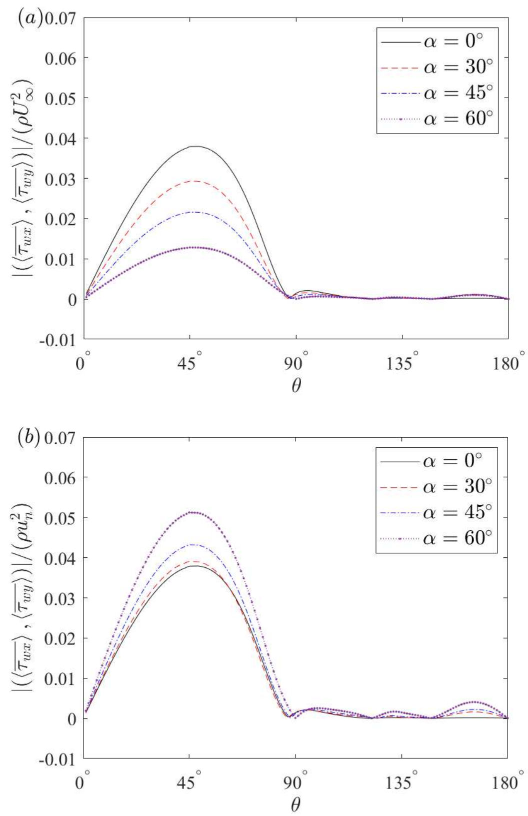

FIG. 16 Tangential wall shear stress component $|(\langle\overline{\tau_{wx}}\rangle, \langle\overline{\tau_{wy}}\rangle)|$ normalized by: (a) free stream velocity U_∞ and (b) normal velocity component u_n.

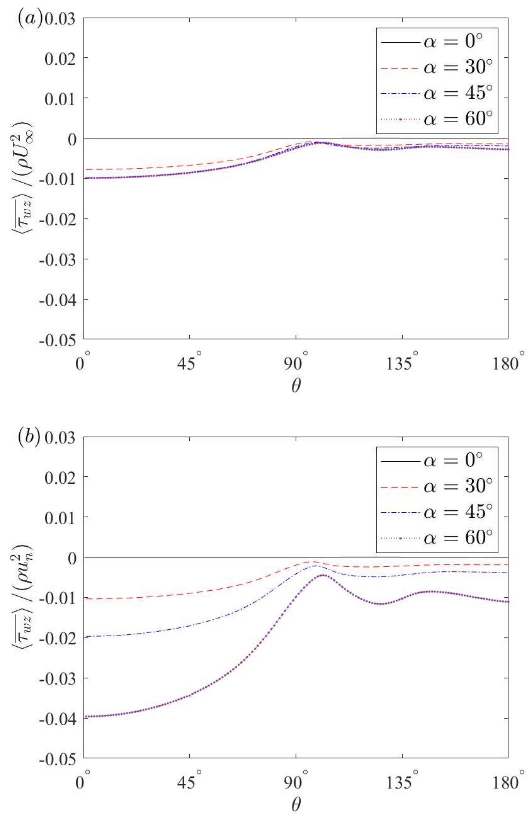

FIG. 17 Spanwise wall shear stress component $\langle \overline{\tau_{wz}} \rangle$ normalized by: (a) free stream velocity U_∞ and (b) normal velocity component u_n.

B. Velocity distribution

The three-dimensional effect in the surrounding flow at different angles of inclination is first illustrated by the averaged results. **FIG. 18** shows the time- and spanwise-averaged velocity component $\langle \bar{u} \rangle$ in the x-axis direction. The recirculation lengths L_{rec}/D (defined by the distance between two points where $\langle \bar{u} \rangle = 0$) are 1.69, 1.84 and 1.69 in the cases of $\alpha = 30^\circ$, 45° and 60° respectively. They are all longer than 1.31, observed in the vertical case. The detailed contours of the velocity component and the averaged streamlines in the x-axis direction in the case of a vertical cylinder are shown in **FIG. 19**, as well as the results in the case of α = 60° representing the inclination cases. In the case of α = 0°, the backward flow behind the cylinder is along the negative *x*-axis direction. While in the inclination case, the spanwise flows occur inside the recirculation zone, which results in the non-zero $\langle\overline{\tau_{wz}}\rangle$ behind the separation point.

The present results can initially explain the difference in drag coefficient $\langle\overline{C_{dn}}\rangle$ among the four cases. In the inclination cases of $\alpha \geq 30°$, the recirculation length is larger than for the vertical case, which leads to an increase in the distance between the cylinder and the location of the lowest pressure indicated by the recirculation core. This results in a higher pressure at the cylinder back ($\theta > 90°$), as shown in **FIG. 13**, and further leads to a lower pressure difference between the front and back sides of the cylinder. It is the root cause of lower drag coefficients in the cases of $\alpha \geq 30°$ compared with the vertical case.

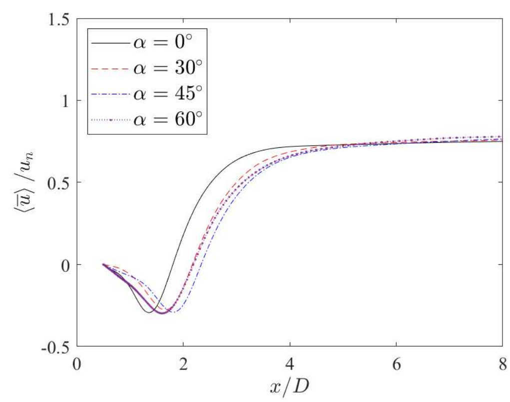

FIG. 18 Velocity component $\langle\overline{u}\rangle$ at $y = 0$.

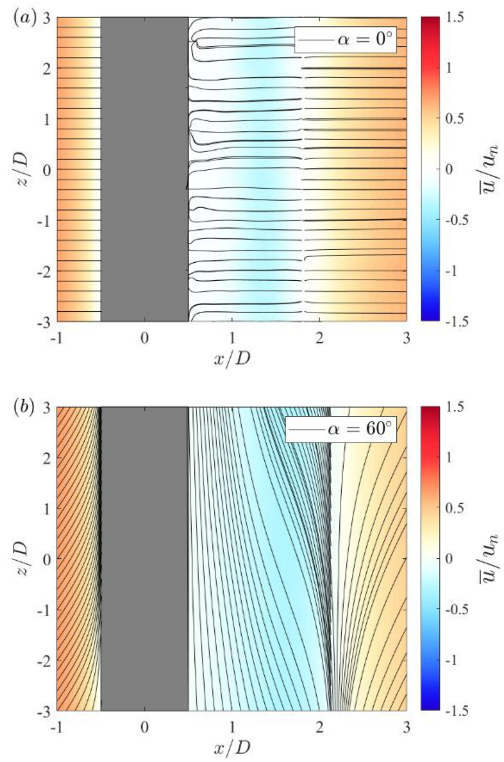

FIG. 19 Streamlines and contours of the time-averaged velocity components $\bar{u}$ at y = 0: (a) α = 0°and (b) α = 60°.

C. Reynolds stress components

The time- and spanwise-averaged Reynolds shear stress distributions in **FIG. 20** provide a quantitative description of velocity fluctuations in the wakes of the analyzed configurations. All the results are normalized using u_n. The locations of the peak values of the Reynolds stress components are similar in three inclination cases. Those locations can also be indicated from the similar lengths of the recirculation zones in three inclination cases in **FIG. 18**, all of which are greater than that in the vertical case. It can be seen from **FIG. 20** that, $\langle \overline{u'v'} \rangle$ is the largest of the three components, and its magnitude decreases with the increasing α. The overall spatial distributions of $\langle \overline{u'v'} \rangle$ are similar for different α. An interesting phenomenon can be observed in the correlations with the spanwise fluctuation w' of $\langle\overline{u'w'}\rangle$ and $\langle\overline{v'w'}\rangle$. Their magnitudes are relatively smaller than $\langle\overline{u'v'}\rangle$, and they increase with the angle of inclination α, while $\langle\overline{u'v'}\rangle$ decreases with increasing α inversely. This observation suggests that with the increase in α, the correlation between u' and v' decreases, while their correlations to the w' are respectively enlarged. With the increasing α within the recirculation region (except for the shear layer region), the amplitudes of $\langle\overline{u'w'}\rangle$ and $\langle\overline{v'w'}\rangle$ increase with α, indicating a strong secondary flow in the spanwise direction induced by the spanwise fluctuations.

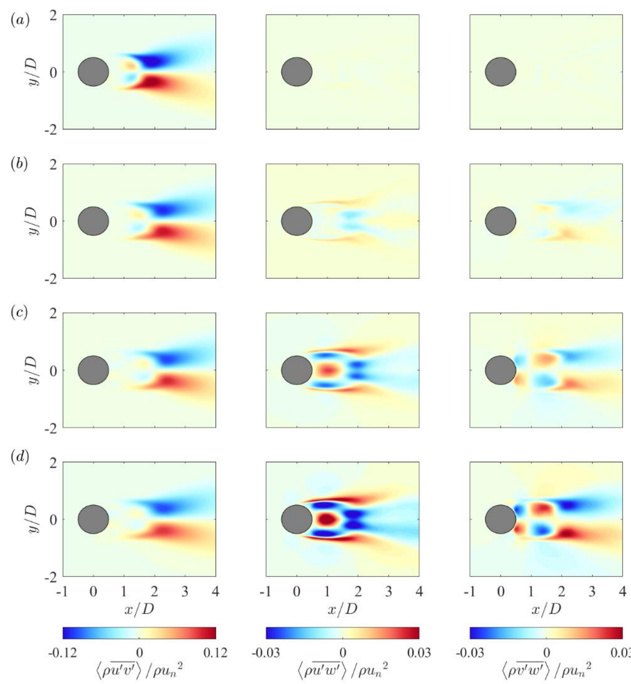

FIG. 20 Reynolds shear stresses: (a) $\alpha = 0°$, (b) $\alpha = 30°$, (c) $\alpha = 45°$ and (d) $\alpha = 60°$, left column is $\langle\overline{u'v'}\rangle$, middle column is $\langle\overline{u'w'}\rangle$ and right column is $\langle\overline{v'w'}\rangle$.

D. Reynolds stress anisotropy

The Reynolds stress shows general variations in turbulent motions in three directions, as explained above. In this sub-section, the Lumley's triangle anisotropy map[26–33] is further employed for quantifying the anisotropy of the Reynold stress. In the following analysis, all the data is sampled along the y-axis, from $y/D = 0$ to $y/D = 6$, as the fluctuations of the wake flow are intense within this range.[33]

In the vertical case of $\alpha = 0°$ in **FIG. 21(a)**, the vortical structures distribution at $x/D = 1$ first shows an oblate shape near $y/D = 0$. As the distance from the centerline increases in y axis, the shape generally changes into a prolate-like shape, accompanied by an increase in anisotropy. At $x/D = 3$, the velocity fluctuation distributions from $y/D = 0$ to $y/D = 6$ are starting from a prolate-like shape, followed by an oblate-like shape, and finally showing an anisotropic prolate shape**.** For the further downstream $x/D = 7$, the vortices at $y/D = 0$ generally display a prolate shape with high anisotropy in the vertical case, and the vortices become two-component axisymmetric disk-shaped in the area near $y/D = 6$. In the case of $\alpha = 30°$ in **FIG. 21(b)**, the variation in the vortices shape is generally similar to that in the vertical case, except that the overall anisotropy is much stronger, especially comparing the flow states at $x/D = 1$. The increasing anisotropy is more evident in the area away from the centerline at $y/D > 2$. Moreover, the occurrence of oblate-shaped vortices at $x/D = 3$ is also closer to the centerline compared with $\alpha = 0°$. The vortex structures at $x/D = 7$ at $y/D = 0$ show a relatively high anisotropy. However, the characteristic shape far away from the cylinder is a one-dimensional line-shaped with high anisotropy, which makes the main difference in vortical anisotropy between the inclined and the vertical cases.

When the angle of inclination further increases to $\alpha = 45°$, the general anisotropy is further enhanced, as shown in **FIG. 21(c)**. The occurrence of oblate-shaped vortices at $x/D = 3$ is less noticeable. For the case of $\alpha = 60°$ in **FIG. 21(d)**, the vortices at $x/D = 1$ generally show the strongest anisotropy, and oblate-shape vortices are less apparent. When the flow state at $y/D = 0$ moves from $x/D = 1$ to $x/D = 3$, the vortices represent an oblate shape, and this shape quickly becomes prolate at $x/D = 3$. This indicates the occurrence of oblate-shaped flow structures is the least obvious in four cases. At downstream area, the vortices become oblate-shaped within a small area near centreline $y/D = 0$ at $\alpha = 45°$, while all the vortices show a prolate- and line-shaped with a high anisotropy in the case of $\alpha = 60°$.

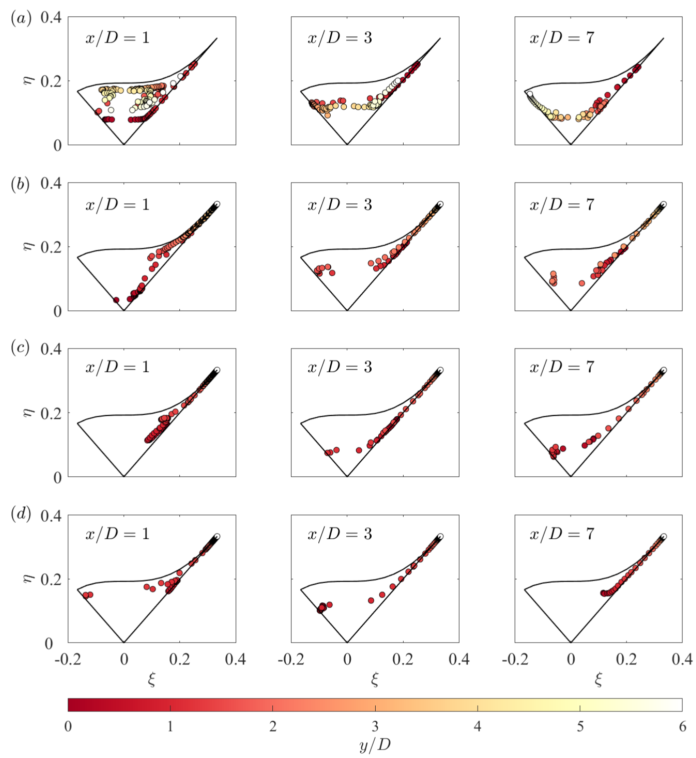

FIG. 21 Lumley's triangles of flow state in y-axis direction sampled at $x/D = 1$, 3 and 7: (a) $\alpha = 0°$, (b) $\alpha = 30°$, (c) $\alpha = 45°$ and (d) $\alpha = 60°$.

In general, the provided Lumley's triangle anisotropy maps reveal that most of the vortices in the near wake of an inclined cylinder are prolate- and line-shaped, especially in the cases of $\alpha = 45°$ and $60°$. It is different from the oblate-shaped vortices commonly observed in the vertical case. Moreover, the oblate-shaped vortex structures also become less apparent in the far wake behind an inclined cylinder. A possible reason is that the vortices are gradually stretched into a long shape with the increasing α and the distance to the cylinder due to the existence of the axial flow and the velocity component in the spanwise direction. Thus, the strength of the vorticity fluctuation is more likely to become pronounced in only one single direction. As a result, all the vortex structures show extreme anisotropy in the area far away from the inclined cylinder with a larger angle of inclination.

E. Spanwise correlation length

In this section, the Hilbert transform is used to quantify the spanwise length scales in the wake of the cylinder. The temporal and spatial variations of the flow structures along the cylinder span at specific locations in the flow field can be studied using this method. Two sampling locations at $y/D = 0$ are selected, as shown in **FIG. 22**.

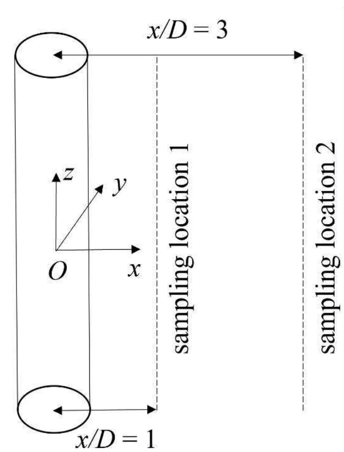

FIG. 22 Sampling locations for spanwise correlation calculation.

The temporal variations of the spanwise length scale λ_z and the amplitude of ω_y at the first sampling location within the recirculation zone are shown in **FIG. 23**. At this location close to the cylinder, the distributions of P_{λ_z} (the PDF of λ_z) are approximately continuous along the temporal axis. High values of P_{λ_z} are correlated with large amplitudes of $\langle C_{ln} \rangle$, which becomes more evident with the increasing α. The highest probabilities are generally located around $\lambda_z/D \approx 0.63$ in all four cases of α. In the low-drag/low-lift regimes, the peak probabilities are much smaller. High values of P_{λ_z} indicate that the vortex structures are well organized and tend to be aligned in similar spatial directions. The results shown in **FIG. 23** suggest that well-organized vortices indicated by high values of P_{λ_z} generally occur with a low pressure in the wake region behind the cylinder. This leads to a high-pressure difference between the front and back sides of the cylinder, which finally results in the high-drag/high-lift regimes as shown in the time histories of $\langle C_{ln} \rangle$ in **FIG. 23** and in **FIG. 14**. Considering A_{ω_y} (the amplitudes of ω_y), it appears that the occurrence of high peaks of A_{ω_y} is further correlated with the occurrence of high P_{λ_z} for the inclined cylinder cases. In the vertical case, the peaks of A_{ω_y} randomly occur both in space and time. When the angle of inclination further increases, A_{ω_y} gradually decreases, indicating the strength of vortices becomes smaller. Moreover, the tilted stripes in the three cases of inclination are due to the spanwise traveling of the vortices near the cylinder. With the increasing α, the tilted stripes become thinner and more sparsely scattered in space and time.

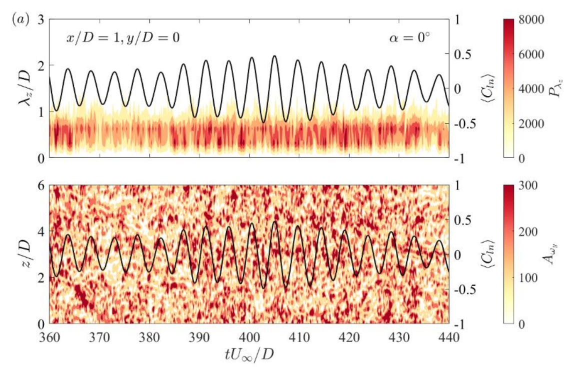

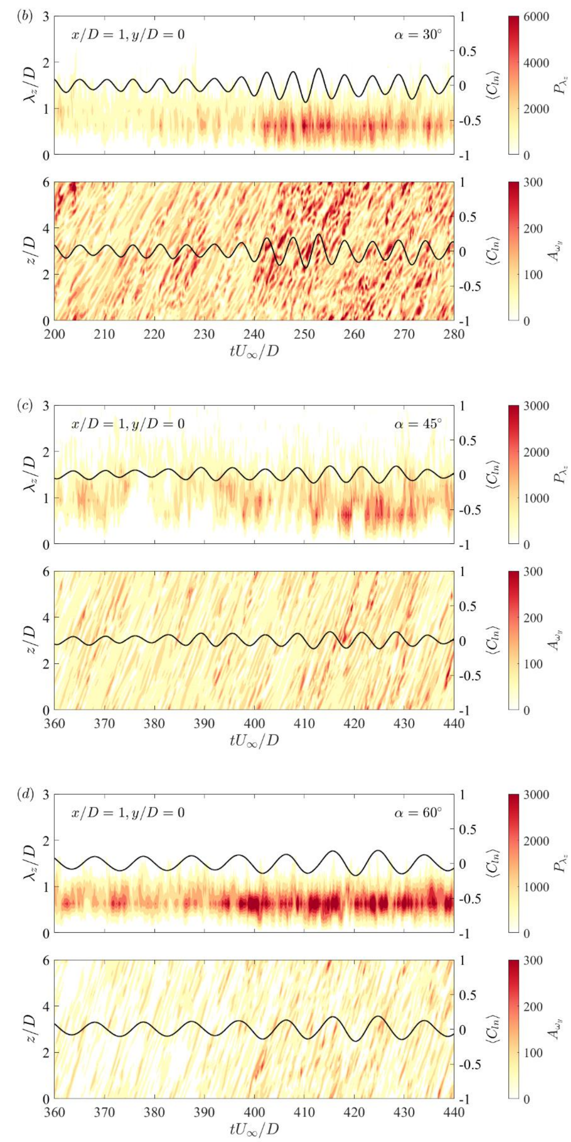

FIG. 23 Probability of length scale P_{λ_z} and amplitude of transverse vorticity A_{ω_y} at $x/D = 1$ and $y/D = 0$, together with spanwise-averaged lift force coefficient: (a) $\alpha = 0°$, (b) $\alpha = 30°$, (c) $\alpha = 45°$ and (d) $\alpha = 60°$.

The vortices outside of the recirculation zone are then analyzed by sampling the data at $x/D = 3$ and $y/D = 0$, as shown in **FIG. 24**. At this location, the peak values of P_{λ_z} and A_{ω_y} periodically occur with the similar frequencies of $\langle C_{ln} \rangle$. This indicates that the vortex shedding behind the cylinder in all four cases of different angles is periodic and may have a major effect on the temporal variations of the forces on the cylinder. The correlation lengths indicated by the peak locations of the P_{λ_z} contours at this location in the four cases are also around $\lambda_z/D \approx 0.63$. On the other hand, A_{ω_y} shows less continuity in the slightly inclined stripes. This suggests that the spanwise traveling of the vortices away from the inclined cylinder is less evident.

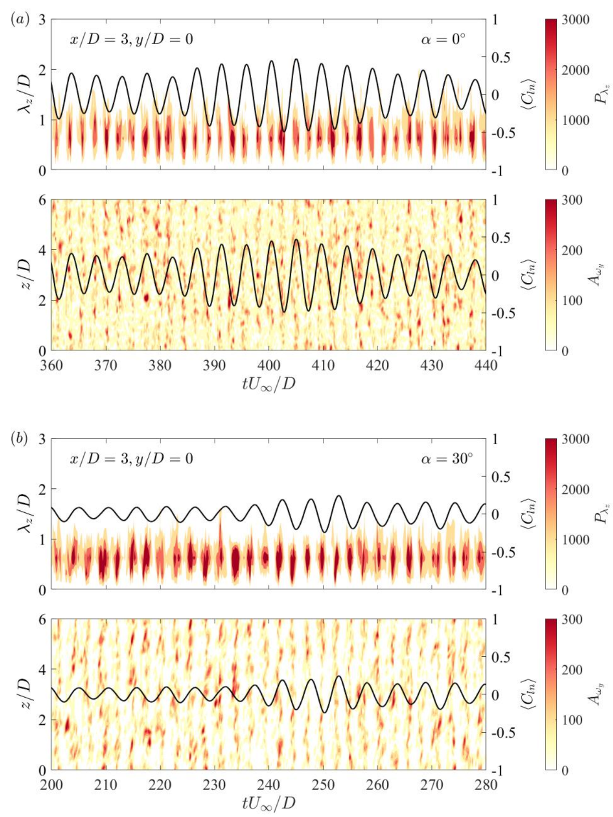

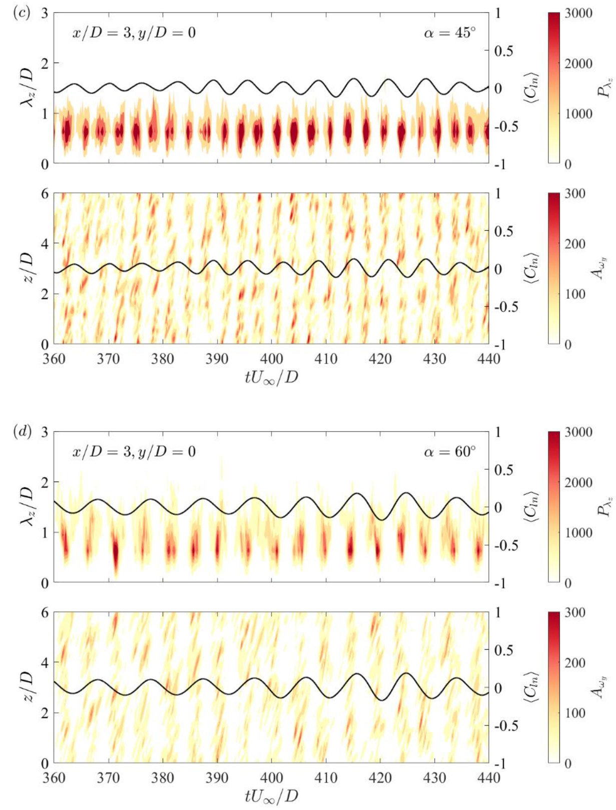

FIG. 24 Probability of length scale P_{λ_z} and amplitude of transverse vorticity A_{ω_y} at $x/D = 3$ and $y/D = 0$, together with spanwise-averaged lift force coefficient: (a) $\alpha = 0°$, (b) $\alpha = 30°$, (c) $\alpha = 45°$ and (d) $\alpha = 60°$.

F. Vorticity contribution to hydrodynamic forces

The above results have shown the differences in the time-averaged and instantaneous flow features observed in the near wakes of cylinders with different angles of inclination. However, it is still of great significance to understand the quantitative correlations between the three-dimensional vortices and the forces on the cylinder at different angles of inclination. Therefore, the force partitioning method[39–43] is adopted to decompose the drag and lift forces into the contributions of the volume integration of the vortices associated with Q and the surface integration of the vorticity on the cylinder due to the viscosity, respectively. Then, the contribution of the vortices in the flow field is further decomposed into the parts of the spanwise vorticity and the cross-spanwise vorticity according to the orientation of the vorticity vector. By analyzing the contours of the vortex-induced forces together with the vortical structures, the quantitative contribution of the vortices can be identified.

FIG. 27 shows an overall view of the time-histories of each force component after spanwise averaging. In the four cases of different inclination angles, the contribution of vortex-induced drag $\langle C_{dn}^{\omega}\rangle$ to the total drag $\langle C_{dn}\rangle$ is higher than 90%. In contrast, the contribution of the viscosity-induced drag $\langle C_{dn}^{v}\rangle$ associated with the vorticity on the surface of the cylinder is approximately less than 5%. Therefore, the force on the cylinder is quantitatively proved to be dominated by the vortices in the wake region, regardless of the angle of inclination. However, when the contribution of the vortices is further decomposed into the parts of spanwise vorticity $\langle C_{dn}^{\omega z}\rangle$ and the cross-spanwise vorticity $\langle C_{dn}^{\omega xy}\rangle$, their contributions to the drag force exhibit noticeable differences for different α. For the vertical case, the dominant factor is $\langle C_{dn}^{\omega z}\rangle$ associated with the spanwise vorticity, and the magnitude of $\langle C_{dn}^{\omega xy}\rangle$ related to the cross-spanwise vorticity is close to zero. The contribution of $\langle C_{dn}^{\omega xy}\rangle$ becomes non-zero for the inclined cylinder cases, and the growth of $\langle C_{dn}^{\omega xy}\rangle$ fluctuations generally synchronizes with the decay of $\langle C_{dn}^{\omega z}\rangle$ fluctuations, as observed in their temporal evolutions. The value of $\langle C_{dn}^{\omega xy}\rangle$ increases and becomes larger than that of $\langle C_{dn}^{\omega z}\rangle$ when the angle of inclination increases to $\alpha = 30°$. As the angle further increases to $\alpha = 45°$, $\langle C_{dn}^{\omega z}\rangle$ gradually becomes the dominant contribution to the vortex-induced drag force again. For the largest investigated $\alpha = 60°$, the cross-spanwise vortex-induced $\langle C_{dn}^{\omega xy}\rangle$ even makes a significant negative contribution to $\langle C_{dn}\rangle$. Considering the lift forces on the cylinder, the vortex-induced lift is also dominant in all four cases, with its contribution accounting for almost the entire lift force. Moreover, the spanwise vortex-induced $\langle C_{dn}^{\omega z}\rangle$ is found to be the main contribution to $\langle C_{ln}\rangle$ in all cases, while the cross-spanwise vortex-induced $\langle C_{ln}^{\omega xy}\rangle$ is out of phase with $\langle C_{ln}\rangle$. Furthermore, with the increasing α, the amplitudes of $\langle C_{ln}^{\omega xy}\rangle$ become comparable to $\langle C_{ln}\rangle$.

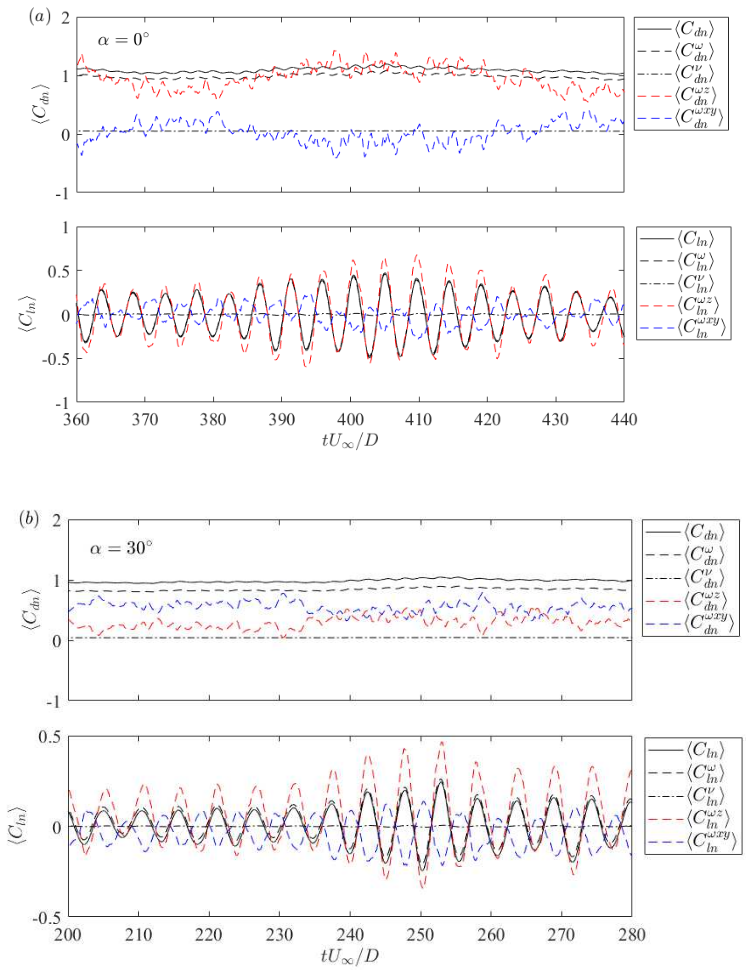
(a)
$\alpha = 0^\circ$
$\langle C_{dn} \rangle$
$\langle C_{dn} \rangle$ $\langle C_{dn}^{\omega} \rangle$ $\langle C_{dn}^{\nu} \rangle$ $\langle C_{dn}^{\omega z} \rangle$ $\langle C_{dn}^{\omega xy} \rangle$
$\langle C_{ln} \rangle$
$\langle C_{ln} \rangle$ $\langle C_{ln}^{\omega} \rangle$ $\langle C_{ln}^{\nu} \rangle$ $\langle C_{ln}^{\omega z} \rangle$ $\langle C_{ln}^{\omega xy} \rangle$
tU_∞/D
(b)
$\alpha = 30^\circ$
$\langle C_{dn} \rangle$
$\langle C_{dn} \rangle$ $\langle C_{dn}^{\omega} \rangle$ $\langle C_{dn}^{\nu} \rangle$ $\langle C_{dn}^{\omega z} \rangle$ $\langle C_{dn}^{\omega xy} \rangle$
$\langle C_{ln} \rangle$
$\langle C_{ln} \rangle$ $\langle C_{ln}^{\omega} \rangle$ $\langle C_{ln}^{\nu} \rangle$ $\langle C_{ln}^{\omega z} \rangle$ $\langle C_{ln}^{\omega xy} \rangle$
tU_∞/D

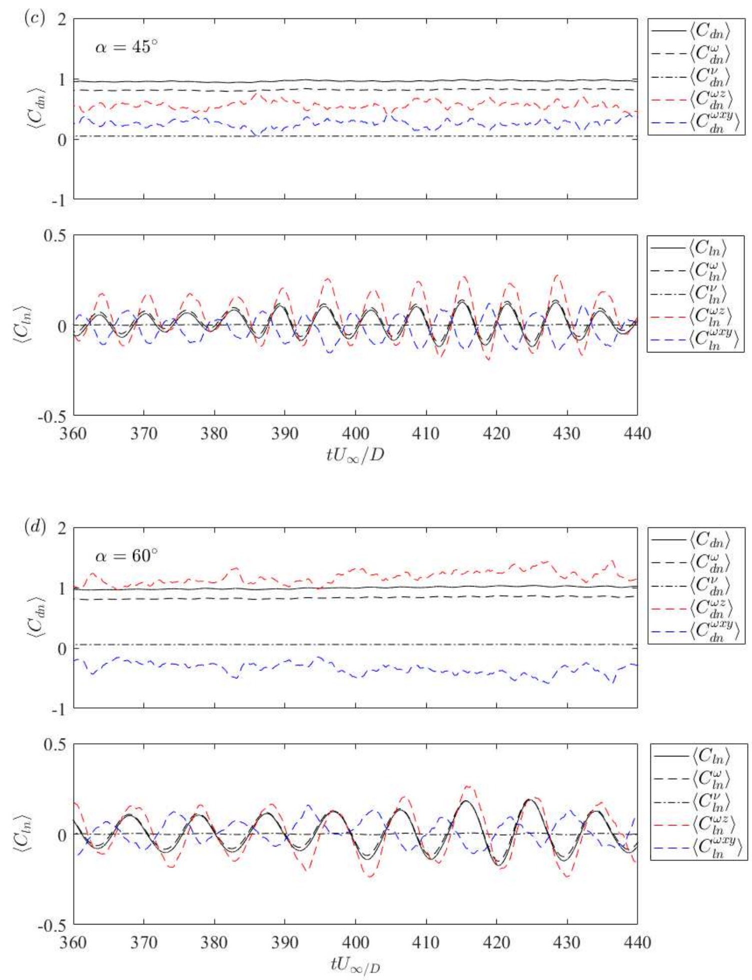

FIG. 25 Force partitioning for spanwise-averaged drag and lift coefficients: (a) $\alpha = 0°$, (b) $\alpha = 30°$, (c) $\alpha = 45°$ and (d) $\alpha = 60°$.

In the following figures, a detailed explanation of the variations in forces is given by plotting the temporal vortex-induced force evolution along the cylinder span. **FIG. 26** shows the decomposed forces in the vertical case of $\alpha = 0°$, together with the spanwise-averaged coefficients. For the dominant component $C_{dn}^{\omega z}$, its magnitude is generally larger than zero, while $C_{dn}^{\omega xy}$ has irregular scattering fluctuations between negative and positive peak values along both the spanwise and temporal directions. This indicates the spanwise vortex formed behind the cylinder can only increase the drag, while the cross-spanwise vorticity can have both positive and negative influence on the drag. The contours of $C_{ln}^{\omega z}$ show clear periodicity with positive and negative magnitudes and $C_{ln}^{\omega xy}$ also displays localized fluctuations with weak temporal periodicity. The peaks of $C_{ln}^{\omega z}$ occur at the same time as troughs of $C_{ln}^{\omega xy}$, and vice versa. This indicates that the cross-spanwise vortices suppress the amplitude of lift force.

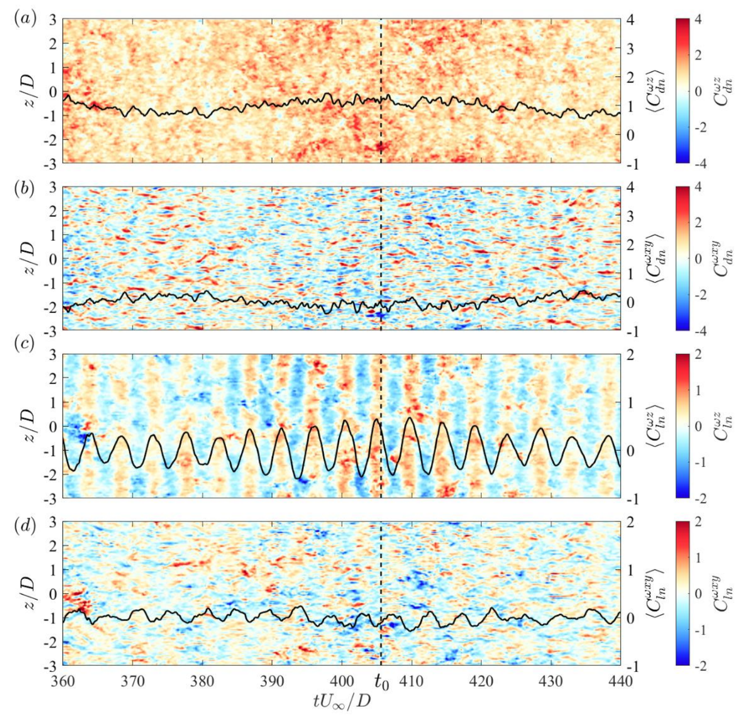

FIG. 26 Temporal and spatial variations in the vortex-induced forces at $\alpha = 0°$: (a) spanwise-vortex induced drag force, (b) cross-spanwise-vortex induced drag force, (c) spanwise-vortex induced lift force and (d) cross-spanwise-vortex induced lift force.

Since the forces on the cylinder have been proven to be highly related to the vortex shedding, the vortex-induced forces on the cylinder are then analyzed together with the three-dimensional vortex structures. **FIG. 27** shows the instantaneous iso-surfaces of spanwise and cross-spanwise vortices at time step $t = t_0$ denoted in **FIG. 26**, colored by their contributions to the vortex-induced force coefficients. For the drag force, the dominant positive contribution of spanwise vortices $-Q_z\varphi_x$ is from the spanwise shear layer, as shown in **FIG. 27(a)**. In the far wake region, the spanwise vortices decay and their influence is less significant. **FIG. 27(b)** shows that for the cross-spanwise vortices, the large contribution to the drag force comes mainly from the highly three-dimensional vortices within the recirculation region. In the far wake region, there are streamwise oriented vortices with a high spatial density. However, their contributions to the drag force are low due to the distance to the cylinder. For the lift force, the contributions of vortices are similar to those observed for the drag force as shown in **FIG. 27(c)** and **FIG. 27(d)**. The only difference is due to the distribution of the potential φ. Therefore, for the other angles of inclination, we only focus on the analysis of the contribution of the three-dimensional vortex-induced drag forces.

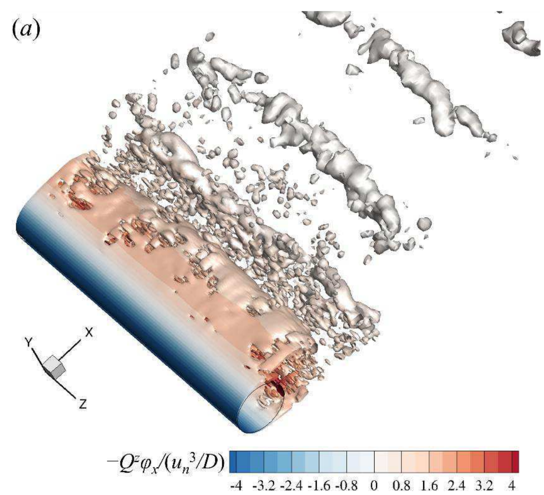

Accepted to Phys. Fluids 10.1063/5.0172540

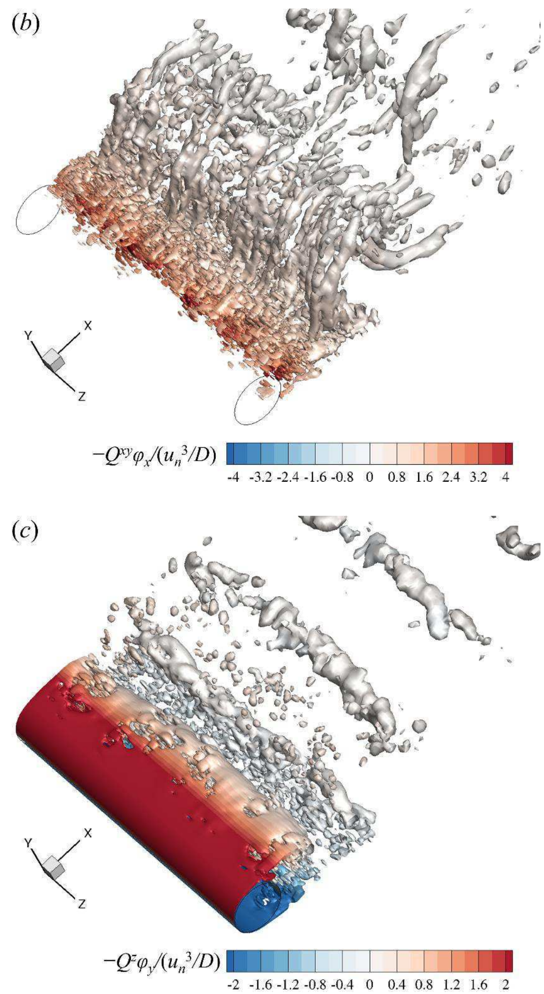

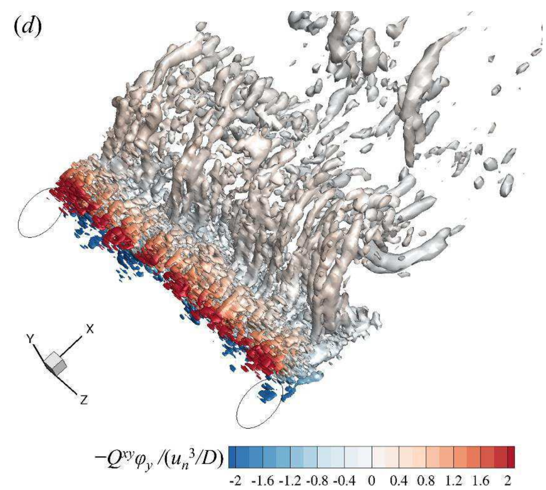

FIG. 27 Instantaneous iso-surfaces of $Q/(U_\infty^2/D^2) = 2$: (a) spanwise vortices colored by $-Q^z\varphi_x$, (b) cross-spanwise vortices colored by $-Q^{xy}\varphi_x$, (c) spanwise vortices colored by $-Q^z\varphi_y$ and (d) cross-spanwise vortices colored by $-Q^{xy}\varphi_y$.

The force decomposition in the inclined case of $\alpha = 30^\circ$ is presented in **FIG. 28**. Different from the vertical case, the overall magnitude of $C_{dn}^{\omega z}$ is much smaller within both low and high drag regimes, while $C_{dn}^{\omega xy}$ time series shows more positive peaks than the corresponding time series for the vertical case. In this study, the spanwise vortices are identified by the angle between the local vorticity vector and the cylinder span being smaller than 45°. Therefore, the increase in the magnitude of $C_{dn}^{\omega xy}$ in **FIG. 28(b)** can be explained by the tilting of spanwise vortices into the cross-spanwise direction. In addition, the stripes in the contours of forces are inclined with respect to the time axis. This indicates the vortices are obliquely traveling along the cylinder span. On the other hand, the vortex-induced lift force at $\alpha = 30^\circ$ shows more temporal periodicity than the vertical case. There are much fewer localized positive peaks in $C_{ln}^{\omega xy}$ compared with those for $\alpha = 0^\circ$ while more negative events of $C_{ln}^{\omega xy}$ than the positive ones, therefore it is indicated that the overall cross-spanwise vortices in this case have a suppressive effect on the lift force.

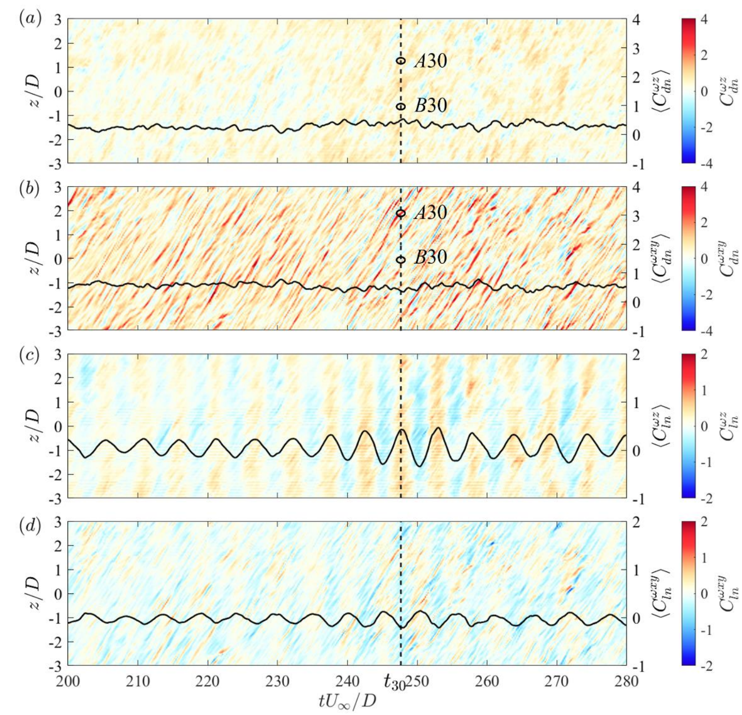

FIG. 28 Temporal and spatial variations in the vortex-induced forces at α = 30°: (a) spanwise-vortex induced drag force, (b) cross-spanwise-vortex induced drag force, (c) spanwise-vortex induced lift force and (d) cross-spanwise-vortex induced lift force.

To provide a three-dimensional view of the vortex structures behind an inclined cylinder, the instantaneous iso-surfaces of the normalized Q at the time step t = t_{30} denoted in **FIG. 28** is shown in **FIG. 29**. The dominant spanwise contribution to drag force $-Q^z\varphi_x$ still comes from the shear layer as shown in **FIG. 29(a)**, while the strength of the shear layer is reduced due to the decreased normal velocity u_n compared with the case of α = 0°. On the other hand, the spatial scales of the spanwise vortices in the near wake become larger compared with those for α = 0°, while their contrition to the drag force is still small. As shown in **FIG. 29(b)**, the contribution $-Q^{xy}\varphi_x$ of the cross-spanwise vortices to the drag force is negative around the stagnation point of the cylinder, which is related to the spanwise motion found in **FIG. 10**. The positive contribution is mainly within the recirculation zone, and it is larger compared with $\alpha = 0°$ case. The spatial scale of the cross-spanwise vortices is larger in the far wake, while their contribution is small due to the distance. A close inspection of the 2D contours on two *xy*-planes at *A*30 and *B*30 is further given in **FIG. 29**, where the contribution of the entire vorticity field is shown. The general contribution of spanwise vortices $-Q^z\varphi_x$ is similar in both contours in **FIG. 29(a)**. It can be also observed that the location where $-Q^z\varphi_x$ reach its maximum occurs approximately at shear layer rollup. These two factors result in a spanwise uniformity of $C_{dn}^{\omega z}$ contours in **FIG. 28**. Due to the strong cross-spanwise vortices at $x/D > 2$ at *A*30 in **FIG. 29(b)**, their contribution to the drag force is high. Compared with *B*30, there are also stronger highly three-dimensional small-scale cross-spanwise vortices within the recirculation region at *A*30. These two factors result in increase of $C_{dn}^{\omega xy}$ at *A*30.

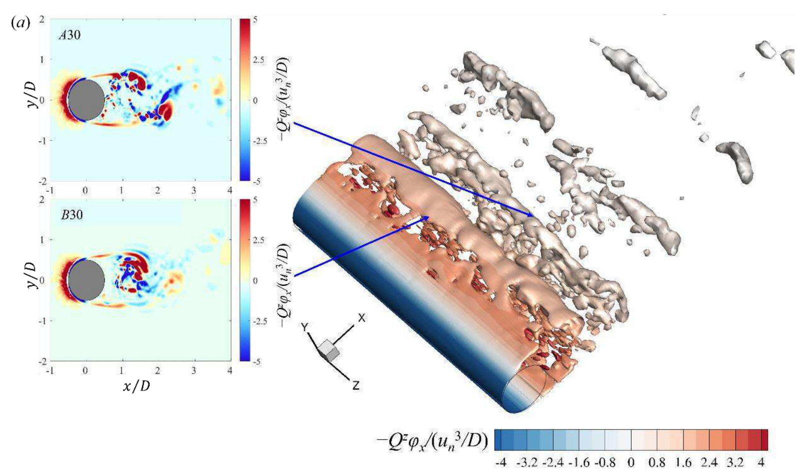

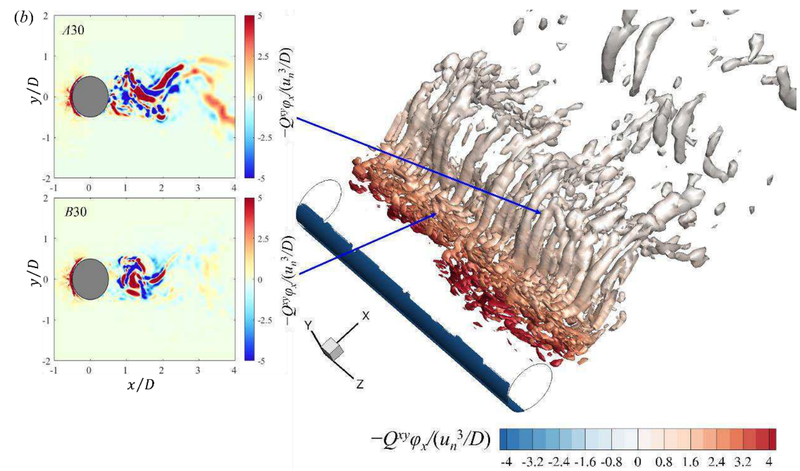

FIG. 29 Instantaneous iso-surfaces of $Q/(U_\infty^2/D^2) = 2$ in the case of $\alpha = 30°$: (a) spanwise vortices colored by $-Q^z\varphi_x$ and (b) cross-spanwise vortices colored by $-Q^{xy}\varphi_x$.

The vortex-induced forces on the cylinder at $\alpha = 45°$ are shown in **FIG. 30**. In comparison against the case of $\alpha = 30°$, the differences in drag forces are that the overall magnitude of $C_{dn}^{\omega z}$ is larger at $\alpha = 45°$, and both strong positive and negative peaks with similar amplitudes occur in $C_{dn}^{\omega xy}$. Considering the lift forces, the general patterns are similar to those observed at $\alpha = 30°$. The only difference is that the variation between the positive and negative peaks is smaller at $\alpha = 45°$. This is also related to the largest distance of the recirculation zone at $\alpha = 45°$ reduces the influence of vortices on the forces.

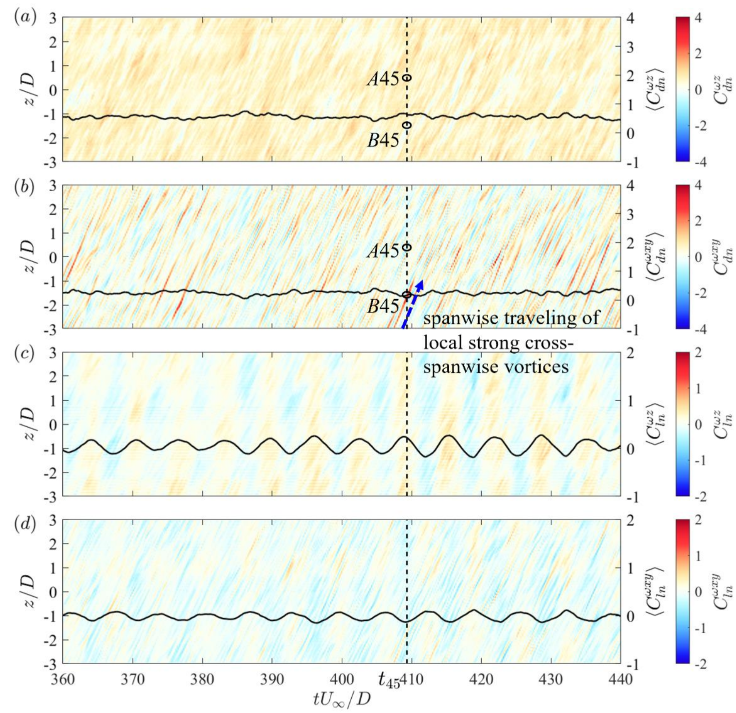

FIG. 30 Temporal and spatial variations in the vortex-induced forces at α = 45°: (a) spanwise-vortex induced drag force, (b) cross-spanwise-vortex induced drag force, (c) spanwise-vortex induced lift force and (d) cross-spanwise-vortex induced lift force.

FIG. 31 shows the iso-surfaces of the vortex structures at $t = t_{45}$. For the spanwise vortices in **FIG. 31(a)**, their spatial density becomes even smaller compared with α = 30°. According to the present instantaneous iso-surface of the normalized Q, the strength of the spanwise shear layer is smaller in comparison with α = 0° and 30°, and thus the main positive contribution to the drag force $-Q^z\varphi_x$ originates from the location of the shear layer rollup. The effect of large inclination angle on cross-spanwise vortices can be seen in **FIG. 31(b)**, specifically vortex structures become aligned in the spanwise direction and well organized. The negative cross-spanwise contribution upstream the cylinder increases with the increasing angle of inclination. Comparing two 2D contours at *A*45 and *B*45, contributions of cross-spanwise vortices at *B*45 are stronger, which results in the intensified positive drag force at the corresponding location. To explain the stripes observed in the force contours, a time-series of 3D cross-spanwise vortices around t = t_{45} is shown in **FIG. 32**. A spanwise traveling of local strong cross-spanwise vortices near *B*45 can be observed as marked by the blue circles. This can be identified as oblique stripes denoted by the blue arrow in **FIG. 30**.

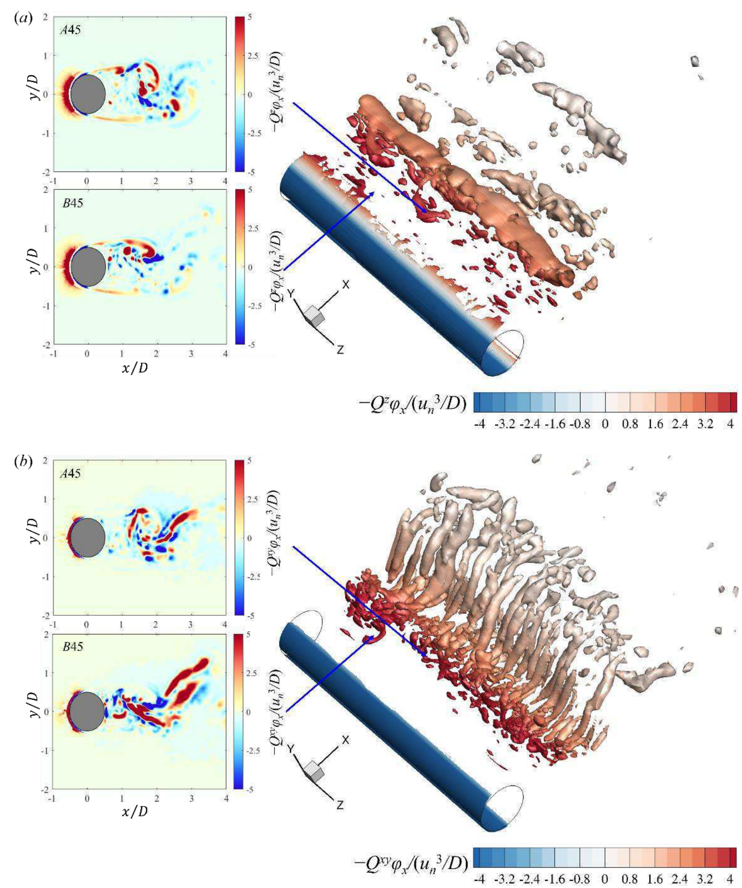

FIG. 31 Instantaneous iso-surfaces of $Q/(U_\infty^2/D^2)$ = 2 in the case of α = 45°: (a) spanwise vortices colored by $-Q^z\varphi_x$ and (b) cross-spanwise vortices colored by $-Q^{xy}\varphi_x$.

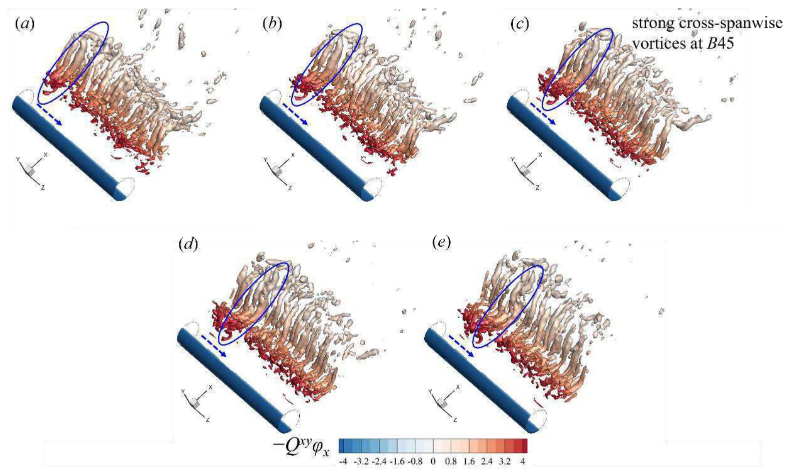

FIG. 32 Instantaneous iso-surfaces of cross-spanwise vortices at $Q/(U_\infty^2/D^2)$ = 2 around t=t_{45} colored by $-Q^{xy}\varphi_x$, (a)~(e) shows the variation in the time sequence.

The results of force partitioning in the case of α = 60° are presented in **FIG. 33**. Considering the drag forces, the overall magnitude of $C_{dn}^{\omega z}$ is positive and is much larger compared with other inclined cylinder cases, while the space-time representation of $C_{dn}^{\omega xy}$ contains predominantly negative values with only a few localized positive streaks. The contributions to the drag force of $C_{dn}^{\omega z}$ and $C_{dn}^{\omega xy}$ are attributed to the change in the spatial organizations of the vortices. Due to the angle of the incident flow, some contributions from the cross-spanwise vortices are extracted and turned into the spanwise direction at α = 60°, which is consistent with the experimental observation in Najafi *et al.*[2] In the time-series of vortex-induced lift force, a clear temporal periodicity for the positive and negative $C_{ln}^{\omega z}$ is visible, and the positive and negative peak values of $C_{dn}^{\omega xy}$ seen as stripes in **FIG. 33(d)** tend to be longer in the spatial-temporal contours compared with other investigated cases.

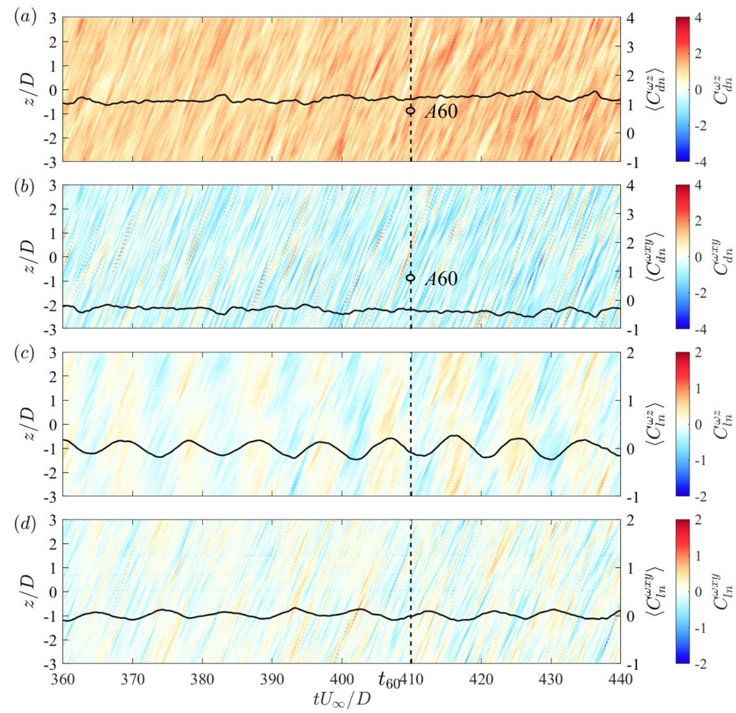

FIG. 33 Temporal and spatial variations in the vortex-induced forces at α = 60°: (a) spanwise-vortex induced drag force, (b) cross-spanwise-vortex induced drag force, (c) spanwise-vortex induced lift force and (d) cross-spanwise-vortex induced lift force.

FIG. 34 presents the instantaneous iso-surfaces at $t = t_{60}$ in the case of α = 60°. As shown in **FIG. 34(a)**, the spanwise uniform vortices in the wake region almost disappear. The vortex structures almost fragment and break down into smaller structures, which is consist with the anisotropy observed in the Lumley's triangle map. Moreover, the strength of the spanwise shear layer indicated by the iso-surfaces of normalized Q significantly decreases with the increasing angle of inclination, and thus its contribution to the drag force almost disappears. The amount of the cross-spanwise vortices also reduces, and their orientation tends to be tilted in the spanwise direction as illustrated on the *xz*-view in **FIG. 34(b)**. Although the cross-spanwise vortices still make some positive contribution to the drag force, due to their low spatial density and a stronger negative contribution around the stagnation point, the overall contribution of $C_{dn}^{\omega xy}$ becomes negative, as observed in **FIG. 33**.

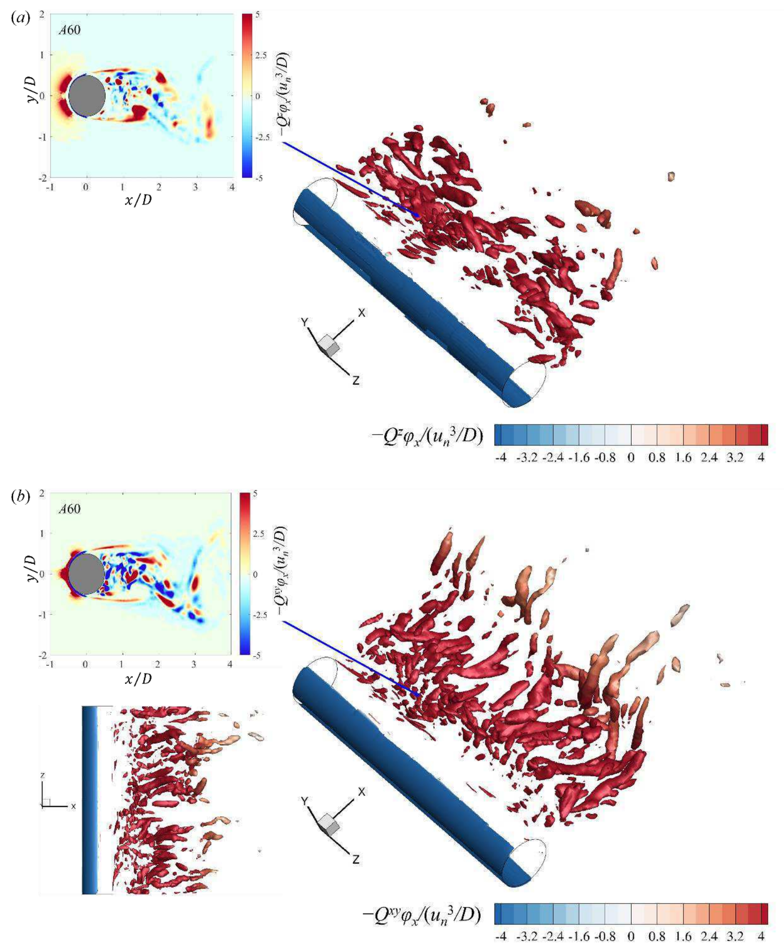

FIG. 34 Instantaneous iso-surfaces of $Q/(U_\infty^2/D^2) = 2$ in the case of $\alpha = 60°$: (a) spanwise vortices colored by $-Q^z\varphi_x$ and (b) cross-spanwise vortices colored by $-Q^{xy}\varphi_x$.

V. Conclusions

The present study utilizes large eddy simulations to investigate the three-dimensional effects of wake flow behind inclined circular cylinder. Initially, a convergence study is conducted at a Re = 3900, aiming to determine the most appropriate grid and temporal resolution. Following the convergence studies, the resultant data from simulations of flow past a vertical cylinder are validated with existing published data. This comparison reveals a good agreement between the present simulations and the published results, in terms of both cylinder pressure and velocity distribution in the wake region. Subsequent investigations involve simulating the flow past inclined cylinders with varying angles of inclination. To simulate the flow past inclined cylinders, the inlet condition is modified to achieve an oblique incoming flow profile. The reliability of this method is further validated by comparing the obtained streamlines and velocity distributions with those in previously published studies. A parametric examination is then conducted, exploring four specific inclination angles of α = 0°, 30°, 45° and 60° at Re = 3900. The validity of the independence principle (IP) is evaluated at different α. In order to explain the origins of discrepancies between the predictions made using IP and the present simulation results, a thorough analysis of the three-dimensional wake features is performed. The main conclusions of the present study are summarized as follows.

1) The vortex shedding frequencies normalized by u_n observed in four cases of inclination angle are similar, and their temporal variations are stable. It appears that IP can be used to predict the Strouhal number of the inclined cylinder flows at Re = 3900 reasonably well. However, both the drag and lift coefficients at $\alpha \geq 30°$ normalized by u_n are smaller than those in the vertical case, indicating deficiencies of IP for predicting force coefficients. It is a consequence of simplifications of the IP method, which is essentially based on a two-dimensional flow and only considers the contribution of the velocities in the cross-spanwise 2D plane. However, the three-dimensional effect induced by the axial flow in the inclination cases cannot be neglected

for larger angles of inclination ($\alpha \geq 30°$). The importance of three-dimensional effects is clearly illustrated by the evolution of the spanwise force coefficient and the magnitude of the spanwise wall shear stress with the angle of inclination.

2) The mean drag coefficient and the r.m.s. lift coefficient normalized by u_n are not decreasing linearly with the increasing α, which is related to the recirculation length L_{rec} of the wake flow. It increases from L_{rec} = 1.31 to L_{rec} = 1.69 with the angle increasing from α = 0° to 30°, reaches its maximum of L_{rec} = 1.84 at α = 45°, and is L_{rec} = 1.69 at α = 30°. With the center of the low-pressure zone moving away from the cylinder, the pressure difference between the front and back sides of the cylinder reduces. Moreover, the variation in vortices also has less influence on the force when L_{rec} increases. These lead to a decreasing $\langle \overline{C_{dn}} \rangle$ and $\langle C_{ln} \rangle_{rms}$ from α = 0° to 45°. With the angle further increases to 60°, L_{rec} decreases, and thus $\langle \overline{C_{dn}} \rangle$ and $\langle C_{ln} \rangle_{rms}$ are larger than those in the case of α = 45°.

3) The force partitioning analysis reveals that both the drag and lift forces on the cylinder are mainly induced by the vortex shedding behind the cylinder, regardless of the inclination angles. Furthermore, the lift force is found to be mainly affected by the vortices in the spanwise direction, while the origins and location of the dominant drag force contributor are highly affected by the angle of inclination. In the vertical case, the drag is mainly caused by the shear layer and the vortices in the spanwise direction. When the angle of inclination is α = 30°, the vortices are mainly in the cross-spanwise direction, and the strength of the spanwise shear layer also decreases. Thus, the cross-spanwise contribution to the drag is larger than that of the spanwise vortices. The strength of the spanwise shear layer further decreases, and the proportions of spanwise and cross-spanwise vortices are similar at α = 45°. Thus, the contributions of spanwise and cross-spanwise vortices to the drag force are of similar magnitudes in the case of α = 45°. When α = 60°, the contribution of the spanwise vortices to the drag increases and the contribution of the cross-

spanwise vortices becomes negative. Since the drag force on an inclined cylinder is highly related to the orientations of the wake vortices, the techniques for modifying the drag on an inclined cylindrical body can be proposed and optimized by modifying the spatial characteristics of the wake vortices in specific directions based on the present conclusion.

4) The spanwise length of the vortices at the centerline is approximately 0.63*D* in all cases of $\alpha = 0°$, 30°, 45° and 60°, whether it is in the recirculation zone ($x/D = 1$) or out of the zone ($x/D = 3$). However, the local strong vortices are found to travel along the cylinder span in all investigated cases, manifested as stripes in the contours of both the amplitude of the vortices and their induced force coefficients. On the other hand, based on the instantaneous iso-surfaces of normalized Q, it is also found that the spatial density of both spanwise and cross-spanwise vortices decreases with the increasing inclination angle. The orientation of cross-spanwise vortices tends to be tilted and the vortex structures in both spanwise and cross-spanwise directions fragment and break down into small structures at $\alpha = 60°$. Moreover, the strength of the vortices is also found to decrease with the increasing angles of inclination according to the amplitude of ω_y. For the characteristic shape of vortices, the vortices are gradually stretched to the prolate shape with the increasing inclination angle, and the vorticity fluctuation is more pronounced in only one single direction, especially for large inclination angles of $\alpha = 45°$ and 60°. These results prove that the vortices display significant anisotropy in the far wake region in the investigated inclination cases.

ACKNOWLEDGMENTS

This study was supported with computational resources provided by UNINETT Sigma 2—the National Infrastructure for High Performance Computing and Data Storage in Norway under Project No. NN9372. The first author also acknowledges the support of the China Scholarship Council (CSC) and the Cultivation Program for the Excellent

Doctoral Dissertation of Dalian Maritime University (2022YBPY002).

DATA AVAILABILITY

The data that support the findings of this study are available from the corresponding author upon reasonable request.

APPENDIX

The detailed results of the convergence study are presented in this section. The convergence test for the mesh is first conducted. **FIG. A1** shows the pressure distribution on the cylinder using coarse, medium and fine mesh of M1, M2 and M3, where the medium and fine mesh show a good agreement. **FIG. A2** shows that the predicted wall shear stress along the cylinder, and the obtained separation points are almost the same using all three meshes. The results of the streamwise velocity component in **FIG. A3** indicates that the medium mesh M2 and the fine mesh M3 capture the same variation in the wake flow field, and further obtain similar recirculation lengths. **FIG. A4** shows the Reynolds stress components at different locations of *x/D* obtained by using the three mesh schemes, where the turbulence characteristics represented by velocity fluctuations are in good agreement by the medium and fine meshes. Based on those results, it can be concluded that M2 has obtained convergence and thus it is used for the following convergence study for the time step.

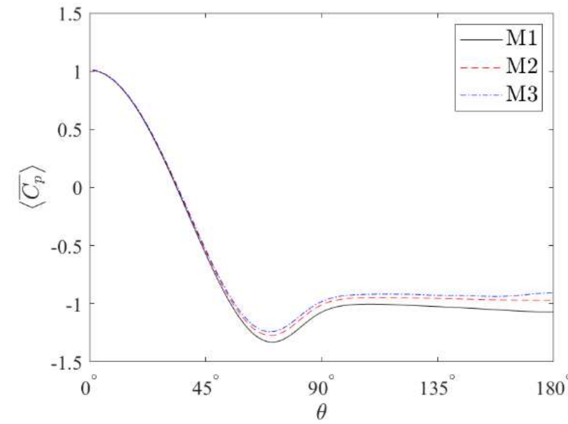

FIG. A1 Convergence study for mesh scheme: pressure coefficient along cylinder.

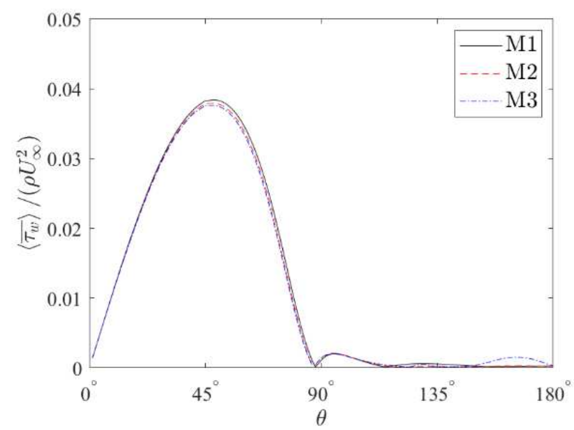

FIG. A2 Convergence study for mesh scheme: wall shear stress along cylinder surface.

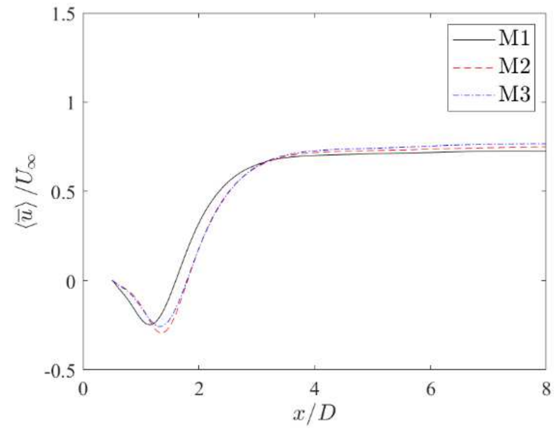

FIG. A3 Convergence study for mesh scheme: velocity component in *x*-axis direction along $y = 0$.

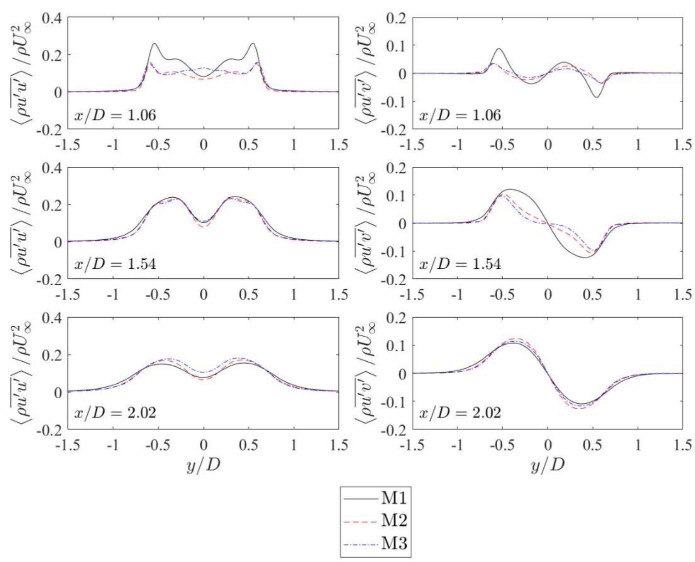

FIG. A4 Convergence study for mesh scheme: Reynolds stress.

The results of the convergence test for the time step are presented in the following figures. **FIG. A5** and **FIG. A6** indicate that the pressure and the wall shear stress along the cylinder are not affected by the variation in the time step. **FIG. A7** shows the streamwise velocity distribution along the centerline $y = 0$, and **FIG. A8** is the velocity fluctuations. The results of T1, T2 and T3 are also in good agreement. Therefore, the mesh scheme M2 and the time step T2 are applied for the rest of the parametric studies considering the balance between the computational cost and the accuracy.

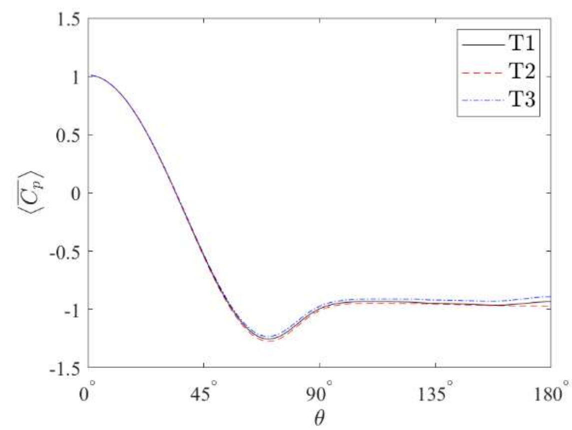

FIG. A5 Convergence study for time step: pressure coefficient along cylinder.

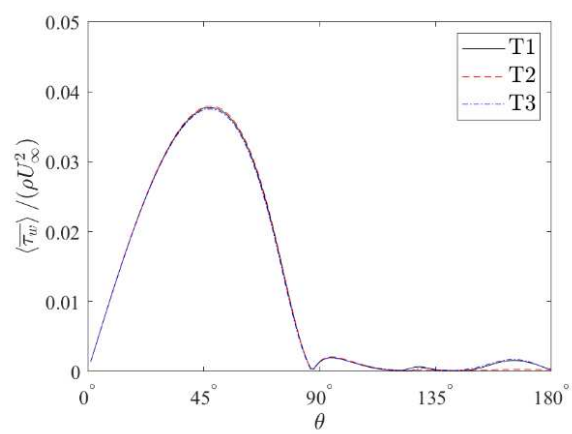

FIG. A6 Convergence study for time step: wall shear stress along cylinder surface.

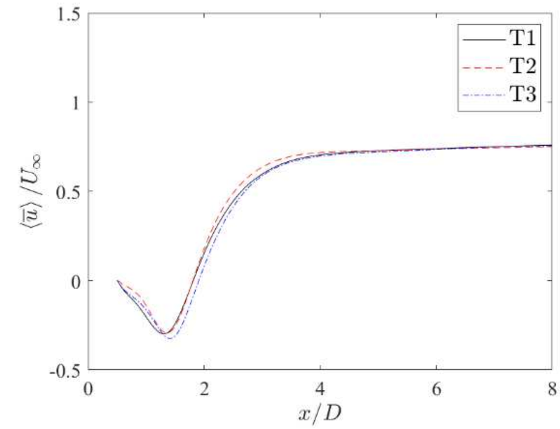

FIG. A7 Convergence study for time step: velocity component in *x*-axis direction along $y = 0$.

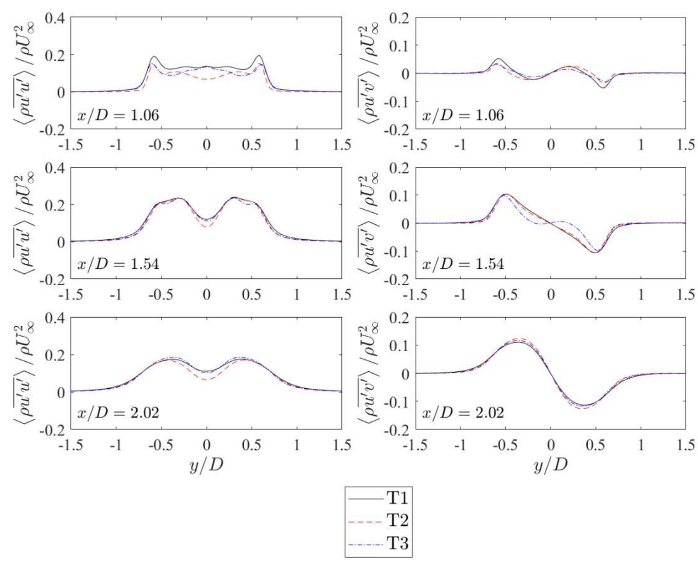

FIG. A8 Convergence study for time step: Reynolds stress.

References

[1] C.H.K. Williamson, "Three-dimensional wake transition," J. Fluid Mech. **328**, 345–407 (1996).
[2] L. Najafi, E. Firat, and H. Akilli, "Time-averaged near-wake of a yawed cylinder," Ocean Eng.

113, 335–349 (2016).

[3] K. Lam, Y.F. Lin, L. Zou, and Y. Liu, "Investigation of turbulent flow past a yawed wavy cylinder," J. Fluids Struct. **26**, 1078–1097 (2010).

[4] S.E. Ramberg, "The effects of yaw and finite length upon the vortex wakes of stationary and vibrating circular cylinders," J. Fluid Mech. **128**(1), 81–107 (1983).

[5] D. Yeo, and N.P. Jones, "Investigation on 3-D characteristics of flow around a yawed and inclined circular cylinder," J. Wind Eng. Ind. Aerodyn. **96**, 1947–1960 (2008).

[6] D. Yeo, and N.P. Jones, "Characterization of flow oblique to a circular cylinder with low aspect ratio using 3-D detached eddy simulation," J. Wind Eng. Ind. Aerodyn. **99**, 1117–1125 (2011).

[7] J.D. Hogan, and J.W. Hall, "The spanwise dependence of vortex-shedding from yawed circular cylinders," J. Press. Vessel Technol. **132**, 031301 (2010).

[8] D. Lucor, and G.E. Karniadakis, "Effects of oblique inflow in vortex-induced vibrations," Flow Turbul. Combust. **71**, 375–389 (2003).

[9] M. Zhao, J. Thapa, L. Cheng, and T. Zhou, "Three-dimensional transition of vortex shedding flow around a circular cylinder at right and oblique attacks," Phys. Fluids **25**, 014105 (2013).

[10] R. Wang, S. Cheng, and D.S.-K. Ting, "Effect of yaw angle on flow structure and cross-flow force around a circular cylinder," Phys. Fluids **31**, 014107 (2019).

[11] S. Zhao, C. Ji, Z. Sun, H. Yu, and Z. Zhang, "Effect of the yaw angle and spanning length on flow characteristics around a near-wall cylindrical structure," Ocean Eng. **235**, 109340 (2021).

[12] A.G. Kravchenko, and P. Moin, "Numerical studies of flow over a circular cylinder at ReD = 3900," Phys. Fluids **12**(2), 403–417 (2000).

[13] C. Lei, L. Cheng, and K. Kavanagh, "Spanwise length effects on three-dimensional modelling of flow over a circular cylinder," Comput. Methods Appl. Mech. Eng. **190**, 2909–2923 (2001).

[14] M.A. Prsic, M.C. Ong, B. Pettersen, and D. Myrhaug, "Large Eddy Simulations of flow around a smooth circular cylinder in a uniform current in the subcritical flow regime," Ocean Eng. **77**, 61–73 (2014).

[15] G. Tian, and Z. Xiao, "New insight on large-eddy simulation of flow past a circular cylinder at subcritical Reynolds number 3900," AIP Adv. **10**(8), 085321 (2020).

[16] H. Jiang, and L. Cheng, "Large-eddy simulation of flow past a circular cylinder for Reynolds numbers 400 to 3900," Phys. Fluids **33**(3), 034119 (2021).

[17] M.J. Janocha, M.C. Ong, and G. Yin, "Large eddy simulations and modal decomposition analysis of flow past a cylinder subject to flow-induced vibration," Phys. Fluids **34**, 045119 (2022).

[18] M. Zhao, L. Cheng, and T. Zhou, "Direct numerical simulation of three-dimensional flow past a yawed circular cylinder of infinite length," J. Fluids Struct. **25**, 831–847 (2009).

[19] R. Wang, D. Xin, and J. Ou, "Three-dimensional characteristics and axial flow pattern in the wake flow of an oblique circular cylinder," J. Wind Eng. Ind. Aerodyn. **206**, 104381 (2020).

[20] M. Zhao, J. Thapa, L. Cheng, and T. Zhou, "Three-dimensional transition of vortex shedding flow around a circular cylinder at right and oblique attacks," Phys. Fluids **25**, 014105 (2013).

[21] H. Liang, and R. Duan, "Effect of lateral end plates on flow crossing a yawed circular cylinder," Appl. Sci. **9**, 1590 (2019).

[22] T. Zhou, S.F.Mohd. Razali, Y. Zhou, L.P. Chua, and L. Cheng, "Dependence of the wake on inclination of a stationary cylinder," Exp. Fluids **46**(6), 1125–1138 (2009).

[23] B. Zhou, J. Wang, G. Jin, Y. Zhou, X. Wang, and W.M. Gho, "Large eddy simulation of flow past an inclined finite cylinder," Ocean Eng. **258**, 111504 (2022).

[24] J.S. Marshall, "Wake Dynamics of a Yawed Cylinder," J. Fluids Eng. **125**(1), 97–103 (2003).

[25] Y. Yuan, H. Xue, and W. Tang, "A numerical investigation of Vortex-Induced Vibration response characteristics for long flexible cylinders with time-varying axial tension," J. Fluids Struct. **77**, 36–57 (2018).

[26] Y. Cheng, L. Fu, S. Dai, M. Collu, C. Ji, Z. Yuan, and A. Incecik, "Experimental and numerical investigation of WEC-type floating breakwaters: A single-pontoon oscillating buoy and a dual-pontoon oscillating water column," Coast. Eng. **177**, 104188 (2022).

[27] Y. Cheng, L. Fu, S. Dai, M. Collu, L. Cui, Z. Yuan, and A. Incecik, "Experimental and numerical analysis of a hybrid WEC-breakwater system combining an oscillating water column and an oscillating buoy," Renew. Sustain. Energy Rev. **169**, 112909 (2022).

[28] F. Nicoud, and F. Ducros, "Subgrid-Scale Stress Modelling Based on the Square of the Velocity Gradient Tensor," Flow Turbul. Combust. **62**(3), 183–200 (1999).

[29] J.L. Lumley, and G.R. Newman, "The return to isotropy of homogeneous turbulence," J. Fluid Mech. **82**(1), 161–178 (1977).

[30] K.-S. Choi, and J.L. Lumley, "The return to isotropy of homogeneous turbulence," J. Fluid Mech. **436**, 59–84 (2001).

[31] N. Hamilton, and R.B. Cal, "Anisotropy of the Reynolds stress tensor in the wakes of wind turbine arrays in Cartesian arrangements with counter-rotating rotors," Phys. Fluids **27**(1), 015102 (2015).

[32] B.F. Garcia, G.D. Weymouth, V.-T. Nguyen, and O.R. Tutty, "Span effect on the turbulence nature of flow past a circular cylinder," J. Fluid Mech. **878**, 306–323 (2019).

[33] Z. Yu, H. Ping, X. Liu, H. Zhu, R. Wang, Y. Bao, D. Zhou, Z. Han, and H. Xu, "Turbulent wake suppression of circular cylinder flow by two small counter-rotating rods," Phys. Fluids **32**(11), 115123 (2020).

[34] M. Emory, and G. Iaccarino, "Visualizing turbulence anisotropy in the spatial domain with componentality contours". In *Center for Turbulence Research Annual Research Briefs*, pp. 123–138 (2014).

[35] F. Michael, *Hilbert Transform Applications in Mechanical Vibration* (Wiley, 2011).

[36] S. Gsell, R. Bourguet, and M. Braza, "Three-dimensional flow past a fixed or freely vibrating cylinder in the early turbulent regime," Phys. Rev. Fluids **3**(1), 013902 (2018).

[37] W. Sarwar, and F. Mellibovsky, "Characterization of three-dimensional vortical structures in the wake past a circular cylinder in the transitional regime," Phys. Fluids **32**(7), 074104 (2020).

[38] M.C. Ong, and G. Yin, "On the three-dimensional wake flow behind a normal flat plate," Phys. Fluids **34**(1), 013603 (2022).

[39] C. Zhang, Mechanisms for Aerodynamic Force Generation and Flight Stability in Insects, Thesis, Johns Hopkins University, 2015.

[40] K. Menon, and R. Mittal, "Significance of the strain-dominated region around a vortex on induced aerodynamic loads," J. Fluid Mech. **918**, R3 (2021).

[41] K. Menon, and R. Mittal, "On the initiation and sustenance of flow-induced vibration of cylinders: insights from force partitioning," J. Fluid Mech. **907**, A37 (2021).

[42] K. Menon, and R. Mittal, "Quantitative analysis of the kinematics and induced aerodynamic loading of individual vortices in vortex-dominated flows: A computation and data-driven approach," J. Comput. Phys. **443**, 110515 (2021).

[43] K. Menon, S. Kumar, and R. Mittal, "Contribution of spanwise and cross-span vortices to the lift

generation of low-aspect-ratio wings: Insights from force partitioning," Phys. Rev. Fluids **7**(11), 114102 (2022).

[44] R. Mittal, and P. Moin, "Suitability of Upwind-Biased Finite Difference Schemes for Large-Eddy Simulation of Turbulent Flows," AIAA J. **35**(8), 1415–1417 (1997).

[45] P. Parnaudeau, J. Carlier, D. Heitz, and E. Lamballais, "Experimental and numerical studies of the flow over a circular cylinder at Reynolds number 3900," Phys. Fluids **20**(8), 085101 (2008).

[46] W. Cheng, D.I. Pullin, R. Samtaney, W. Zhang, and W. Gao, "Large-eddy simulation of flow over a cylinder with a skin-friction perspective," J. Fluid Mech. **820**, 121–158 (2017).

[47] H. Liang, and R. Duan, "Effect of Lateral End Plates on Flow Crossing a Yawed Circular Cylinder," Appl. Sci. **9**, 1590 (2019).

[48] X. Ma, G.-S. Karamanos, and G.E. Karniadakis, "Dynamics and low-dimensionality of a turbulent wake," J. Fluid Mech. **410**, 29–65 (2000).